



**Characterization of 2D Jammed Granular
Memristive Copper Arrays**

THESIS

Len L. Kedrow, Captain, United States Air Force
AFIT-ENP-MS-15-M-073

**DEPARTMENT OF THE AIR FORCE
AIR UNIVERSITY**

AIR FORCE INSTITUTE OF TECHNOLOGY

Wright-Patterson Air Force Base, Ohio

DISTRIBUTION STATEMENT A
APPROVED FOR PUBLIC RELEASE; DISTRIBUTION UNLIMITED

The views expressed in this document are those of the author and do not reflect the official policy or position of the United States Air Force, the United States Department of Defense or the United States Government. This material is declared a work of the U.S. Government and is not subject to copyright protection in the United States.

AFIT-ENP-MS-15-M-073

CHARACTERIZATION OF 2D JAMMED GRANULAR MEMRISTIVE COPPER
ARRAYS

THESIS

Presented to the Faculty
Department of Engineering Physics
Graduate School of Engineering and Management
Air Force Institute of Technology
Air University
Air Education and Training Command
in Partial Fulfillment of the Requirements for the
Degree of Master of Science

Len L. Kedrow, BS
Captain, United States Air Force

25 March 2016

DISTRIBUTION STATEMENT A
APPROVED FOR PUBLIC RELEASE; DISTRIBUTION UNLIMITED

AFIT-ENP-MS-15-M-073

CHARACTERIZATION OF 2D JAMMED GRANULAR MEMRISTIVE COPPER
ARRAYS

Len L. Kedrow, BS
Captain, United States Air Force

Committee Membership:

Alex Li, PhD
Chair

Ronald A. Coutu Jr., PhD
Member

Marina Ruggles-Wrenn, PhD
Member

Abstract

A novel sensor made of jammed granular memristive copper spheres was explored in an effort to develop a protection technology that could be used in non-proliferation treaty monitoring. The $700\mu m$ copper spheres used in the device were annealed at $100^\circ C$ for 5, 15 and 30 minutes. SEM, EDS, and XPS were used to characterize the growth of the oxide coating. The SEM images showed a similar morphology to the un-annealed spheres for all three of the samples. EDS showed the three samples of spheres had similar stoichiometry of 10% Oxygen 90% Copper, while the XPS peak areas were $Cu^0 = 80\% \pm 2\%$, $Cu^{+1} = 6\% \pm 1\%$, and $Cu^{+2} = 14\% \pm 3\%$, which showed the oxide thickness was similar in the three samples. Electrical characterization of the device was done by confining the granular copper spheres to a two-dimensional plane using a unique test fixture capable of measuring I-V curves at the boundary of the sphere plane with pillar electrodes made of tungsten. electroforming of the copper spheres broke down the oxide later and created conductive filaments. It was shown that the conductivity of the filaments could increase, by reduction of the copper oxide using a field-driven process. Similarly, the conductivity of the filament decreased via oxidation assisted by Joule heating. The affects of mechanical force on the conductive filaments were also studied. The Conductive conductive filaments were easily broken with 22mN steps of force, but remained intact longer when 5.6mN steps were used. The changes in the conductive filaments could be used as a detection mechanism for an electromechanical sensor.

AFIT-ENP-MS-15-M-073

To my Monkey and Little Man. May my actions be a template for your success and my faults be examples of what to avoid in life.

Acknowledgements

This work would not have been possible without the following individuals. First my committee, Dr. Alex Li, you never spoon fed me the answers, but gave me the freedom to make discoveries for myself. Dr. Marina Ruggles-Wrenn, your door was always open, and your no-nonsense mentoring showed me that I can do anything. Dr. Ronald A. Coutu, your words were few, but their affect were great. I thank you all. Furthermore, the knowledge I obtained in XPS could not have been done without Dr. Tony Kelly and Dr. David Turner. I also owe Dr. Turner many thanks for his time improving my understanding of chemistry. I was once told that a good Materials Scientist needs a good Machinist; Brian Crabtree and the Kid in the AFIT machine shop were mine. There were several challenges to create the final test fixture used in this research, and these two individuals assisted me with solving them. The Game Night Guys, thanks for keeping me sane between measurements in the lab. Robbyn Turner, my writing therapist, COMM 680 showed me how to enjoy writing, which was something I feared. Finally, to the Zens master, no one person gave more of their personal time than you. The energy you put into my education has caused a permanent phase change that will remain until my passing.

Len L. Kedrow

Table of Contents

	Page
Abstract	iv
Acknowledgements	vi
List of Figures	ix
List of Tables	xi
I. Introduction	1
1.1 Motivation	1
1.2 Research Objective	2
1.3 Previous Research	5
1.4 Scope	6
1.5 Thesis Organization	7
II. Review of Literature	8
2.1 Memristor Theory and Early History	9
2.2 Memristor Operations	11
2.3 Nucleation and Diffusion	14
2.4 Copper Oxides	17
2.5 Summary	20
III. Methodology	21
3.1 Copper Spheres	21
3.2 Test Fixture	22
3.3 Experimental Set-Up	24
3.4 Force Chains and Conductive Filaments	26
3.5 Summary	32
IV. Results and Analysis	33
4.1 Oxide Composition	33
4.2 Initialization and Test Procedure	40
4.3 Constant Force Measurements	43
4.4 Varied Force Measurements	51
V. Conclusion	55
5.1 Overview	55
5.2 Oxide Growth	55
5.3 Conductive Filament Formation	55

	Page
5.4 Two-Dimensional Jammed Memristive Copper Sensor	56
5.5 Future Work	57
Appendix A. Logic Tables of Varied Force Measurements 22mN steps.....	59
Bibliography	61

List of Figures

Figure		Page
1.1	3D sensor cross section	3
1.2	Graphical representation of planar and spherical memristors	4
1.3	1D Test Rig	5
1.4	2D Test Rig with Elector Pads	7
2.1	Planar Memristor Structure	8
2.2	Illustration of the four circuit theory variables and their six relationships. Graphic from [1]	9
2.3	Example of Pinched Hysteresis Loop	10
2.4	electroforming Effects	12
2.5	Restive Switching Diagrams	14
2.6	Free-energy change ΔG vs radius	15
3.1	Illustration of sphere location in furnace during annealing	22
3.2	Test Fixture One	23
3.3	Physical and graphical representations of the second test fixture	24
3.4	Experimental Set-Up Labeled	25
3.5	Forming Memristive Force Chains	27
3.6	Copper Filament Growth Due to Radius	29
3.7	Force effect on conductive filaments	30
3.8	15 Min Sample Mounted for XPS	32
4.1	SEM data for annealed spheres	34
4.2	A typical SEM interaction volume of signal events	35
4.3	Time Elapsed-Binding Energy	36

Figure	Page
4.4	<i>Cu2p_{3/2}</i> XPS Spectrums 37
4.5	Normalize <i>Cu2p_{3/2}</i> XPS Spectrums for 5, 15 and 30 min samples 39
4.6	Floating spheres due to static charge on the copper oxide thin film 39
4.7	Various Annealed Sphere Samples 100°C and 200°C 40
4.8	Graphical Representation of sensor 41
4.9	Constant Force Electrode (0,4) 46
4.10	Constant Force Electrode (0,3) 47
4.11	Constant Force Electrode (0,2) 48
4.12	Constant Force Electrode (0,1) 49
4.13	Constant Force Electrode (0,a) 50
4.14	Mean Value Plots for 5 Minute Samples 52
4.15	30 Minute Mean Negative ON Values 5.6mN Steps 54

List of Tables

Table		Page
1	Copper Sphere Specifications	21
2	Cantilever Characteristics	26
3	EDS Data of Copper Spheres	34
A.4	Logic ON OFF Chart for Annealed Sphere Samples	60

CHARACTERIZATION OF 2D JAMMED GRANULAR MEMRISTIVE COPPER ARRAYS

I. Introduction

1.1 Motivation

The United States (US) has continued to modernize its nuclear weapon infrastructure since President Kennedy first issued National Security Action Memo No. 160 [2]. This memo ordered nuclear weapons to be under positive US control using technical means. One technical area of consideration is system protection technologies. A large number of system protection technologies are used to provide an adequate level of security. Protection technologies range from network intrusion detection systems, which monitor activity and send alerts when suspicious traffic is detected, to complex security systems monitoring doors and windows over several buildings. A novel protection technology made of granular memristive material will be studied to understand how it could be used to sense and store information regarding mechanical or electrical manipulation. By understanding how the granular memristive material reacts to mechanical or electrical stimulation, devices could be created to provide tampering histories for Weapons of Mass Destruction (WMD).

System protection technologies play an important role in non-proliferation treaty monitoring and the protection of WMD from unauthorized use or abuse [2]. Current technologies in use implement “use control,” which are security measures that prevent unauthorized access. [3] Several components implement use control such as Coded Control Device (CCD), Command Disablement System (CDS), Active

Protection System (APS), and Permissive Action Link (PAL). The APS is the only protection technology which detects physical attacks on the WMD and responds by causing damage to critical components, rendering them useless. The damaged component is left with no data that can be used to provide information about the attack. A new sensor capable of retaining information about attacks would improve the level of protection and assist with monitoring for nonproliferation compliance.

1.2 Research Objective

The goal of this research is to establish a novel sensor that can detect intrusion via mechanical or electrical means using a jammed granular memristive system. The final sensor system will consist of a granular material of randomly-packed spheres. The memristive characteristics of the sensor will be configured in accordance with application and user requirements.

Granular materials are made of a large number of particles, which interact via surface forces. Sand, rice, and coffee beans are all examples of granular materials. For this research, the granules will be copper spheres with a diameter of approximately $700\mu m$. It has been argued that granular materials could be their own state of matter, due to their unique behavior that is not seen in solids, liquids, or gases [4]. One of these behaviors is observed when a granular material is stored in a cylindrical container. The pressure at the bottom of the container is not dependent on height of the granular material, as it would be with a fluid. The lack of dependence is due to force being transmitted through the granules' contact points, which form a force network [4]. This force network is made up of force chains that carry the load [5]. Force chains are segments of three or more granules with correlated direction and intensity [6]. A description of how force chains are generated is included in Chapter III. The red line in Figure 1.1b shows the force

chains that are constructed, as the plate has force applied. The creation and destruction of force chains is key in forging the Metal/Insulator/Metal (MIM) structure needed to form a memristive network that can be used for mechanical and electrical sensing.

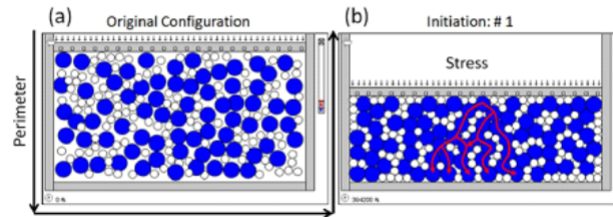


Figure 1.1. This figure shows the formation of a two-dimensional granular network, composed of binary spheres, before and after mechanical stress is applied in the y-axis direction, (a) is the original configuration with the particles loosely packed forming small chains. (b) After a mechanical stress is applied, the binary spheres compress and create a network of force chains in the sensor.

The memristor is a two-terminal passive circuit element, with resistance values dependent on the magnitude, direction, and duration of the applied voltage [7]. This change in resistance is maintained even after power has been removed from the memristor, giving the memristor a memory characteristic. As was mentioned above, the initial MIM structure used to create a memristor is a thin insulative material sandwiched between metal contacts. The contact point between two oxidized copper spheres will provide the MIM structure needed to create a memristor. This is a drastically different structure than the planar devices that are the focus of most research being done. Figure 1.2 is a graphical representation of the planar memristor configuration found in most literature and the spherical memristor configuration used in this thesis. The annealed spheres will be confined into a two-dimensional plane until they they are in contact. The confined spheres form random sets of memristive force chains through their contact points. The MIM structures in the force chains can be initialized through a process called

“electroforming,” which will be discussed in Chapter II.

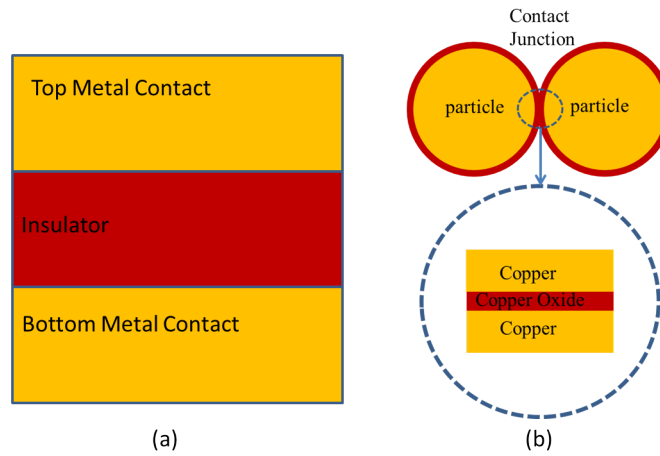


Figure 1.2. (a) Is the traditional memristor construction using metal as the top and bottom electrodes with a layer of insulative material separating them. (b) Is the configuration that will be used in this thesis. Starting with pure copper spheres, the insulator is grown on the outside in the form of copper oxide. When two spheres come in contact, they form the Metal/Insulator/Metal configuration needed to make a memristor.

The memristive force chains’ configuration is unique, and its electrical output is only known to the individual who set it; therefore, if electrical manipulation occurs, the resistance of the memristive chains will be altered. This resistance change can be monitored by an external system and alert the user. Likewise, if physical intrusion is attempted, the position of the spheres will be altered, breaking the memristive force chains and forming new ones. The change in memristive chains will have a new resistive signature, and the user can be alerted again. The key to furthering the development of this sensor requires a solid understanding of how its signature will change with mechanical or electrical manipulation.

1.3 Previous Research

Previously, one-dimensional jammed granular memristive systems were studied by Orta and Willey for their response to electrical excitation dependent on mechanical loading [1, 8]. Copper spheres similar to those used in this research were etched using nitric acid before being oxidized on a hotplate in open air for various periods of time. After being treated, the spheres were put through several tests by Orta and Willey, with Orta focusing on electrical characterization and Willey investigating mechanical perturbations [1, 8]. These experiments used chains of various lengths confined to a capillary tube with one fixed tungsten electrode and a second tungsten electrode mounted on a computer-controlled stage to provide measured displacement. Figure 1.3 provides a view of the one-dimensional test fixture and a chain of three copper spheres under test.

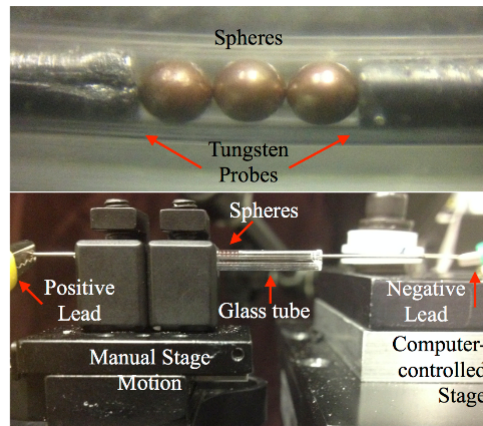


Figure 1.3. The picture shows a zoomed-in view of a three-sphere chain on top, and the bottom contains a view of the test set-up used during the 1D testing by Orta and Willey. Picture from [1].

During Orta's research, a breakdown voltage of 10V per sphere in chain was found in spheres oxidized for five minutes without being etched and under no load [1]. This value was cut in half for etched spheres. The etched spheres were also shown to have less hysteresis, as the oxidation time increased. During sphere sample

compression, hysteresis increased with oxide thicknesses with an approximately linear trend [8]. The longer the spheres' oxidation time, the higher rate of compression could occur before reaching dielectric breakdown. The effects of oxide thickness on sensitivity and resiliency indicated an important design trade off that will be considered during two-dimensional testing.

1.4 Scope

The scope of this research is to leverage what has been learned from the one-dimensional system and use it to design and characterize a two-dimensional system. A thin oxide coating will be grown on copper spheres using thermal oxidation. The oxide coating will be analyzed using X-Ray Photoelectric Spectroscopy (XPS), Energy Dispersive Spectroscopy (EDS), and a Scanning Electron Microscope (SEM). How electrical properties are influenced by mechanical force will be studied using a unique test fixture. Figure 1.4 is a bird's-eye view of the first test fixture used in this study. A fiberglass base with electrode pads and a plastic top will be used to confine the plane of spheres. Plastic plates will be used to vary the force the spheres are subjected to from approximately 0-220mN. The study will include considering how memristive force chains and conductive filaments, created during electroforming, respond when force is varied. The growth and decay of the conductive filaments, due to field-driven oxidation and reduction at constant force, will also be examined. Chapter III will discuss the testing process used to modify the test fixture to its final configuration.

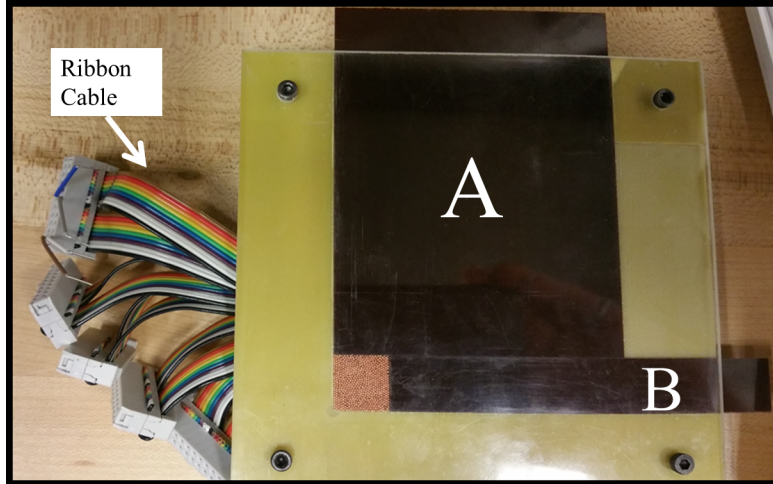


Figure 1.4. Two-dimensional test fixture used to isolate copper spheres into a plane. The copper spheres are placed into a $75\text{mm} \times 75\text{mm}$ well and covered with a plastic plate. Walls to confine the copper spheres are created by Plate A, which is held constant and Plate B, which is used to apply force. After initialization, the spheres I-V responses were taken using ribbon cable connected to electro-pads embedded into the test fixture.

1.5 Thesis Organization

This thesis will continue in Chapter II with a literature review of memristor theory and stable copper oxides. Next, Chapter III will provide the methodology used to conduct the experiments. Followed by Chapter IV, which will address experiment findings and analysis techniques. Finally, Chapter V will conclude the thesis and identify recommendations for future work.

II. Review of Literature

This chapter will consist of a detailed look at the materials and methods used to characterize the two-dimensional granular memristive sensor being researched in this thesis. The chapter starts with a brief look at memristor theory. As was mentioned previously, the memristive devices described in this chapter are of the planar construction, which are different from the spherical configuration used in this research. The planar devices consist of a Metal/Insulator/Metal (MIM) construction, in which the different materials are layered, similar to a sandwich, with the metal contacts being the bread and the insulators the filling. Figure 2.1 illustrates two general configurations of planar devices using one or two different insulators. The chapter continues with a discussion of the stable copper oxides, and how they can be grown using thermal oxidation. This chapter will conclude with a measurement method that can be used to quantify the abundance of copper species present in the oxide shell.

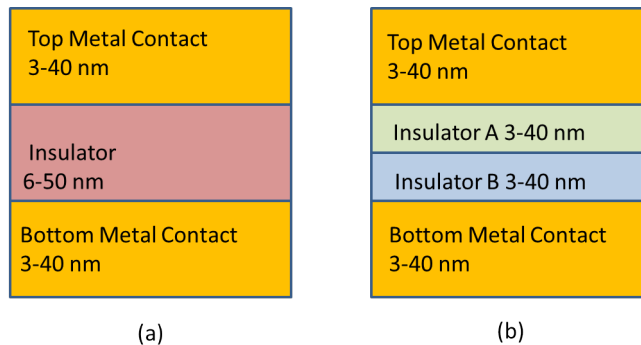


Figure 2.1. Generic memristors in using the planar Metal/Insulator/Metal structure showing (a) single-insulator configuration and (b) double-insulator configuration. Insulator A and B could be different oxides, organic material, or a combination among other insulators. Adapted from [1].

2.1 Memristor Theory and Early History

In 1971, Leon Chua proposed the existence of a fourth passive circuit element. The memristor, named by Chua, is a portmanteau of memory and resistor, because it acts like a nonlinear resistor with memory [9]. Chua's theory was based on a missing component in the symmetry of the fundamental circuit theory variables and their mathematical relationships. The four fundamental variables of circuit theory are voltage, electric current, magnetic flux, and charge. Chua showed that the fundamental variables had six possible mathematical relationships, but that only five existed in linear circuit theory. Three of these equations were defined by the two-terminal passive circuit elements: the resistor, capacitor, and inductor. The final two equations were given as $i = \frac{qd}{dt}$ and $V = \frac{\varphi d}{dt}$.

There was no equation or circuit element that described the relationship between charge and flux. Chua showed mathematically that a passive circuit element should exist, whose value changed based on the amount of flux that passed through the device. Figure 2.2 is a graphical representation of the fundamental circuit theory variables and their six relationships in their nonlinear systems form.

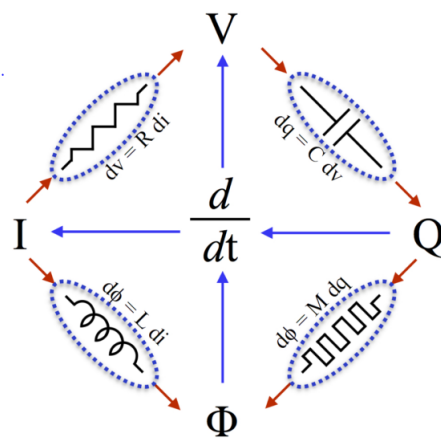


Figure 2.2. Illustration of the four circuit theory variables and their six relationships. Graphic from [1]

Chua demonstrated that the missing component could be described by a nonlinear relationship between the current and voltage modeled as

$$V(t) = M(q(t))i(t) \tag{1}$$

where $M(q(t))$ is memristance, a nonlinear function of charge that can be described as resistance at a particular point in time [9].

In 1976, Chua worked with Sung Mo Kang to generalize memristor theory to a class of dynamic devices called memristive systems [10]. In their paper, Chua and Kang listed general properties of a memristor. These properties described the Lissajous figure produced from a single cycle of a small AC signal. The Lissajous figure is often referred to as a pinched hysteresis loop [7]. The pinched hysteresis loop must pass through the origin, and the hysteresis loop's frequency response causes it to degenerate into a linear time-invariant resistor, as the excitation frequency tends towards infinity [10]. Chua and Kang's theory was mathematically rigorous but contained no insight regarding a physical device that could be called a memristor. It would take another 35 years before HP Labs connected their research on a platinum (Pt) and titanium oxide (TiO_2) MIM devices to Chua's theory [7].

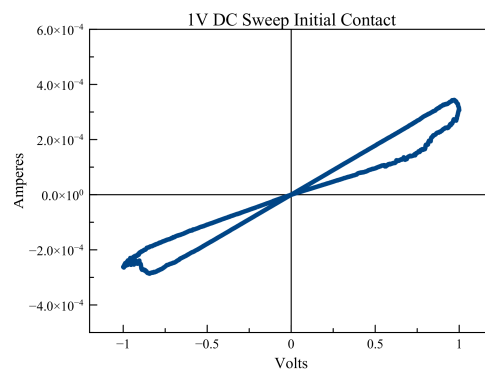


Figure 2.3. Example of Pinched Hysteresis Loop

Pinched hysteresis loop captured during preliminary reading made on a 1D chain of 10 spheres

In 2006, HP Labs was seeking an answer to the inconsistent results they were receiving from their Pt/TiO/Pt memory devices when they came across Chua’s papers, which discussed the pinched hysteresis loops. [7]. HP Labs used Chua’s theory to provide physical insight about how the memristor functioned by connecting Chua’s mathematical proofs to their data. These connections led to a series of papers, which laid the foundation of modern memristor theory [11, 12, 13, 14]. One of the key discoveries was a physical mechanism of coupled electron-ion dynamics showing that positive oxygen ion migration turned conductive paths on or off depending on the bias voltage polarity [12, 11]. HP’s discovery of a physical device sparked research on several topics in an effort to fully characterize the mechanisms of memristors. Many of these device functions were established with research but were not well understood. The next section of this chapter explains the device operations of the electroforming process and dynamic resistance switching.

2.2 Memristor Operations

This section departs from a chronological review to a topical discussion on the operational characteristics of the memristor. The section starts with the electroforming process that is needed to turn a pristine device from a high-resistance state to a low-resistance state for the first time. A review of different switching mechanisms follows the electroforming review.

2.2.1 Electroforming

When a MIM device is constructed, its resistance value is large due to the electrical properties of insulators [15]. A high voltage, $V_{forming}$, must be applied across the device to initially put it into a low-resistance state [7]. This process is called “electroforming” and is necessary to cause a soft breakdown that forms

conductive paths in the memristive device [11, 16]. Fujiwara demonstrated the creation of a bridge in a M/CuO/M device, where the metal used was either copper or nickel [16]. When the bridge was cut in the M/CuO/M study, the device returned to its original resistance showing that the bridge was responsible for providing the conduction path. The temperature dependence, before and after forming, suggested that the bridge contained pure copper filaments, whose lengths were increased or decreased through reduction and oxidation. Fujiwara also showed that hard break down could occur if $V_{forming}$ was too large. Figure 2.4 shows the different states that could occur in the M/CuO/M devices [16].

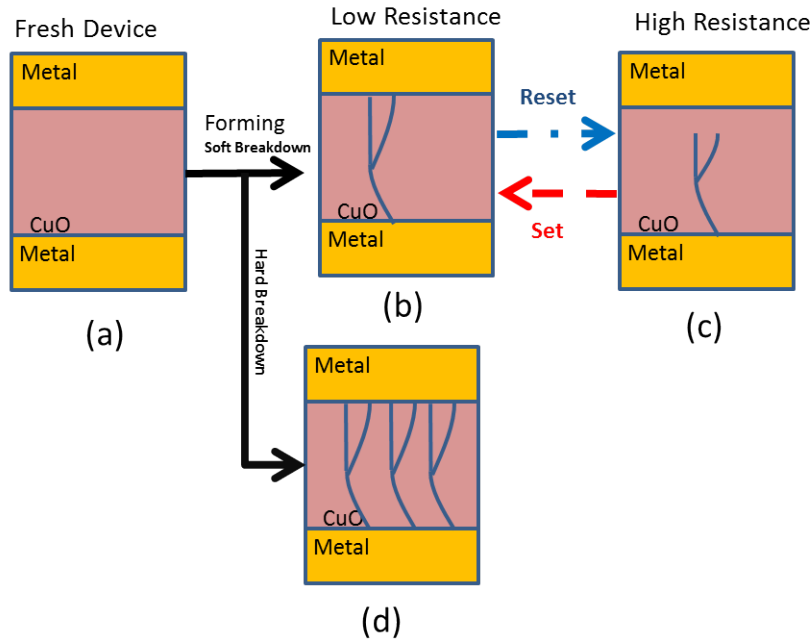


Figure 2.4. This diagram shows (a) pristine device can have (b), (c) soft breakdown forming a single conductive filament, capable of low or high resistance, or (d) hard break down forming multiple conductive filaments. Adapted from [16]

Memristive devices are often inconsistent after the forming process, which makes it difficult to use them in designing new circuits [17]. Due to this randomness, memristive devices have been constructed not to require electroforming and

demonstrate more consistent device characteristics [7]. HP labs restructured their device after finding that the initial layer of TiO_2 had separated into two layers –an oxygen-rich layer of TiO_2 and a thinner layer that was oxygen deficient of TiO_{2-x} [11]. HP labs also determined they did not need electroforming, if the layer of TiO_2 was reduced to a few nanometers thick. More recently, Auburn University used an ink jet printer to build a Cu/CuO/(AgO)/Ag memristor that did not require electroforming to operate [18]. By standardizing the performance of a MIM memory device, they could be incorporated into circuits, which would reduce the number of transistors needed and decreases the power required. After a memristive device has been electroformed, voltages lower than $V_{forming}$ can be used to toggle the resistance from a high-resistance state to a low-resistance state using setting voltage called V_{set} and from a low-resistance state to a high-resistance state using a reset voltage called V_{reset} . The toggling is called “restive switching” and can occur in different modes.

2.2.2 Restive switching

The ability for a memristor to change its resistance based on the magnitude, direction, and duration of the applied voltage makes this device attractive for electronic applications. The change in resistance is referred to as “restive switching” and has been documented to occur in two modes: unipolar and bipolar [17]. This is different from Chua’s theory, which only predicted bipolar switching. In unipolar switching, V_{set} and V_{reset} can have the same polarity, because the switching is only dependent on the amplitude. For bipolar switching, V_{set} and V_{reset} , the switching is dependent on polarity; therefore if V_{set} is a positive voltage then, V_{reset} will be a negative voltage and vice versa. Figure 2.5 is a graphical representation of the two switching modes. There have been reported cases of memristive devices that show both modes of switching and are referred to as “non-polar switching” [17].

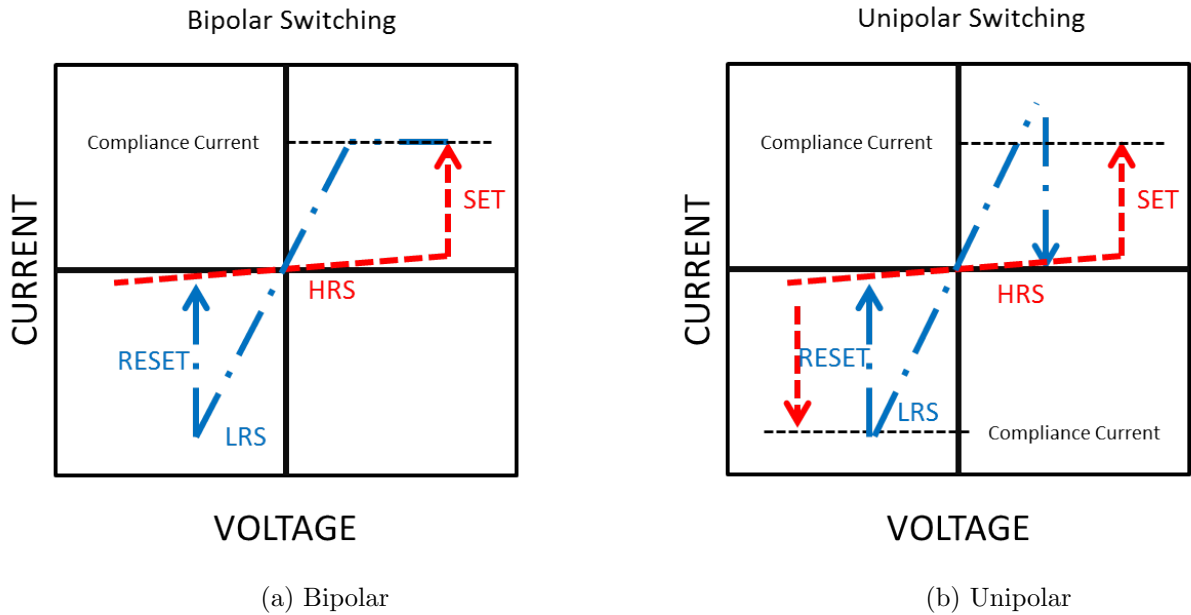


Figure 2.5. (a) shows I-V example plot of bipolar switching, and (b) shows I-V example plot of unipolar switching. Adapted from [17]

2.3 Nucleation and Diffusion

2.3.1 Homogeneous Nucleation

Homogeneous nucleation is the phase transformation of a material, such as liquid to solid or gas to liquid, in the bulk of a fluid material when significant under-cooling has occurred [19]. The initial nuclei are formed by the cooled atoms, which bond together to form unstable embryos, or stable nuclei depending on their radius; it is assumed the crystals form in spherical particles for solids. The stability of the crystals are dependent on the relationship of the radius to the total free energy change ΔG_T . The total free energy is the sum of two competing energies: the change in the bulk free energy, ΔG_v also called the “*driving energy*,” and the “*retarding energy*” ΔG_s , which is the surface-free energy of the particle γ times the area of the particle’s surface. The total free energy change for a spherical crystal

is modeled with Equation 2

$$\Delta G_T = \frac{4}{3}\pi r^3 \Delta G_v + 4\pi r^2 \gamma \quad (2)$$

Figure 2.6 shows the plots of ΔG_v , ΔG_s , and ΔG_T . changing with the radius r . At the critical radius r^* , ΔG_v reaches a maximum ΔG_r^* . If the crystal radius is less than r^* , it is referred to as an embryo, which will redissolve and reduce the energy in the system. However, if r is greater than r^* , the particle is called a nuclei which will continue to grow due to growth driving a decrease in the system's energy. Although homogeneous nucleation is difficult, due to the ΔG_r^* energy barrier that must be overcome, the concept can be used as a tool to discuss filament growth in Chapter IV.

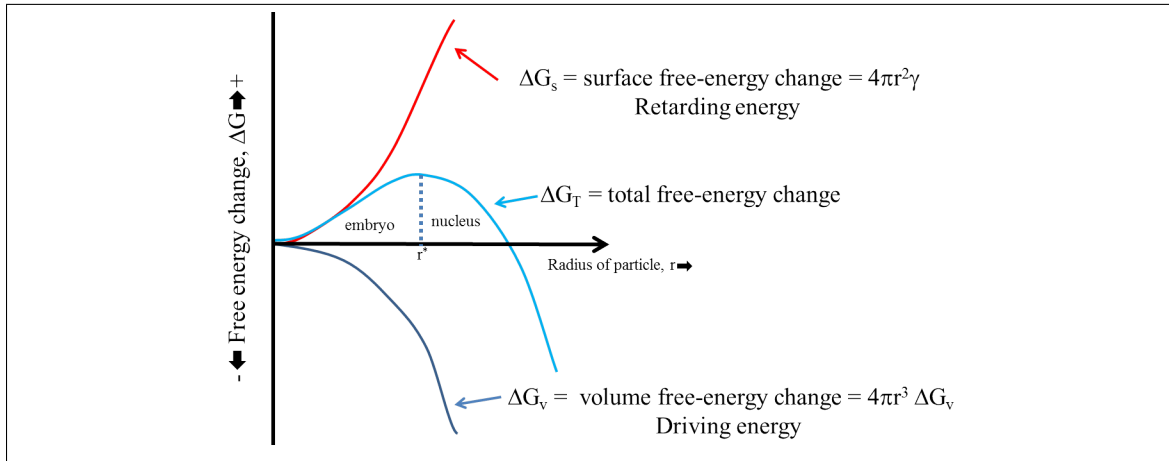


Figure 2.6. This graph illustrates the free-energy change vs radius. When r is greater than r^* , a nucleus forms; if less than r^* , an embryo forms. Adapted from [19]

2.3.2 Diffusion

“Diffusion can be defined as the mechanism by which matter is transported through matter” [19]. This transport is facilitated either by the substitutional mechanism or the interstitial mechanism. The substitutional diffusion arises when an atom can move from one lattice site to another due to the presence of sufficient

activation energy and vacancies in the lattice. Interstitial diffusion occurs when an atom moves from one interstitial site to a second interstitial site without permanently affecting any of the other atoms. The size of the interstitial atom must be smaller than the matrix atom.

Diffusion is described mathematically by Fick's First and Second Laws. Fick's First Law is for the steady-state diffusion condition of the flux, J , or flow of atom, which is proportional to the diffusivity coefficient, D , times the concentration gradient, $\frac{dC}{dx}$, and can be represented in one dimension by Equation 3.

$$J = -D \frac{dC}{dx} \quad (3)$$

The negative sign is placed on the right-hand side of the equation, because the diffusion gradient is negative, but the flux is a positive number. Fick's Second Law is a linear differential equation, which provides the transient concentration, $\frac{dC}{dx}$, as a system moves toward steady state, which may never be reached. Fick's Second Law in one dimension is give by Equation 4.

$$\frac{\partial C}{\partial x} = D \frac{\partial^2 C}{\partial x^2} \quad (4)$$

The value of the diffusivity coefficient is dependent on several factors [19]. As the temperature at which diffusion takes place increases, so does diffusivity. The crystal structure of the material being diffused will play a role due to atomic packing factor variations and the lattice spacing. As previously mentioned, interstitial or substitutional mechanism also plays a role in diffusivity. Like nucleation, understanding diffusion and how its rate can be affected can be very useful, when discussing conductive filament growth in the memristive force chains.

2.4 Copper Oxides

Copper is the transition metal used for both the metal contacts and the metal oxide insulator in the MIM structure of the 2D granular memristive sensors being characterized in this research. This section examines the stable forms of copper oxides (Cu_xO) that occur in nature and their electronic structure. Also, the use of thermal oxidation to grow thin film copper oxides will be discussed.

2.4.1 Stable Oxides

Copper oxides occur naturally in three forms. Alternatively, thin copper oxide films (Cu_xO) can be grown using multiple methods [20]. Cupric Oxide (CuO), also called Cu^{2+} , has a black color and a monoclinic lattice structure. Cu^{2+} has an open d shell, $3d^9$, which leads to shake-up peaks in XPS Spectrum. Shake-up peaks will be discussed in detail later in this chapter. Cu^{2+} is a p-type semiconductor with a reported band gap range of 1.2 to 2.16 eV. Cuprous oxide Cu_2O , also called Cu^{1+} , is the second stable oxide. Cu^{1+} has a reddish color and cubic lattice structure; its d shell, $3d^{10}$, is full. Cu^{1+} is also a p-type semiconductor and has a band gap of 2.1-2.6 eV. Cu_4O_3 is the final stable version of copper oxide, which is a mixture of CuO and Cu_2O . Cu_4O_3 is the least studied of the three oxides and belongs to the tetragonal lattice structure. The band gap of Cu_4O_3 has been reported in the range of 1.34 to 2.47eV [20].

2.4.2 Cu_xO Growth by Thermal Oxidation

“Thermal oxidation is a method where thin oxide films are grown directly on the surface of a Cu substrate, when the substrate is exposed to high temperatures” [20]. One study examined the annealing of copper in the atmosphere at temperatures up to $1000^{\circ}C$ and reported the phase evolution of raw copper to Cu^{2+} [21]. Pure Cu_2O

films were measured at $200^{\circ}C$, and transition to CuO was observed between $250 - 275^{\circ}C$. Finally, uniform CuO was seen above $300^{\circ}C$.

2.4.3 Determining Ratios of Copper(I)/Copper(II) using XPS

XPS is a surface analysis technique for defining the elemental composition of a solid's outer surface within the first 10nm. Electrons initially bound to the atoms are ejected by an x-ray photon. The x-ray photon is annihilated during photon-electron interaction with complete energy transfer occurring. If the energy is sufficient, the electron will escape the solid, and its kinetic energy ($K.E.$) will be measured. These K.E. values can be converted to binding energy ($B.E.$) using the following formula [22]:

$$K.E._{XPS} = E_{photon} - \phi_{XPS} - B.E._{XPS} \quad (5)$$

where ϕ_{XPS} is the work function of the system. Spectra of these $B.E._{XPS}$ can be analyzed to identify and quantify the element composition of the solid's surface and reveal the chemical environment in which the elements exist.

When determining the chemical state of copper solids, the 2p spectra is used, but similar $B.E._{XPS}$ for Cu (932.61eV) and Copper (I) (932.43eV) make identification difficult [23]. Due to this tight value between the $B.E._{XPS}$ energy of Copper and Copper(I) electrons, the $K.E._{XPS}$ values of the Cu LMM Auger peaks are used to identify the presence of the three different species. The Auger peaks are found by subtracting the $B.E._{XPS}$ from E_{photon} and are located at Cu (918.5eV), Cu^{2+} (917.7eV), and Cu^{1+} (916.7eV). Once the question of what species are present has been answered, this data can be used to properly fit the 2p_{3/2} peak and quantify the amount of each species present, using the method developed by Jaseniak and Gerson and described in [24].

The method Jaseniak and Gerson developed is dependent on the shake-up structure of the copper spectrum. Shake-up peaks are formed when an already-excited electron leaving the solid interacts with a bound valance electron. This interaction transfers energy or “shakes up” the valance electron; if the excitation is great enough, this valance electron will also escape and be detected, but its energy level will be shifted to a lower $K.E.XPS$, which is seen as a higher $B.E.XPS$ peak in the spectrum [24]. Use of this shake-up peak is an important requirement in determining the amount of copper species present in a solid.

The method to determine the surface ratio of Cu^{1+}/Cu^{2+} is dependent on obtaining a ratio of the main peak area, ($A_{100\%}$), to the shake-up area, ($B_{100\%}$), for a pure 100% Cu^{2+} sample. Once the Cu^{2+} ratio has been determined, the relative concentration of both Cu^{1+} and Cu^{2+} present in the surface layer can be determined using the following equations:

$$\%Cu^{1+} = \frac{A_2}{A+B} \times 100 = \frac{A - A_1}{A+B} \times 100 = \frac{A - (\frac{A_{100\%}}{B_{100\%}})}{A+B} \quad (6)$$

$$\%Cu^{2+} = \frac{B + A_1}{A+B} \times 100 = \frac{B(1 + (\frac{A_{100\%}}{B_{100\%}}))}{A+B} \times 100 \quad (7)$$

where B is the area of the shake-up peak and A is the total area of the main peak of the analyzed sample. Figure 4.3b shows a spectrum of the copper $2p_{3/2}$ spectrum of a planar sample that Castle annealed for 15 minutes in a 50/50 Oxygen/Argon environment [25]. The XPS spectrum has both Cu^{1+} and Cu^{2+} peaks represented. The peaks have been labeled to assist with understanding Equations 6 and 7.

2.5 Summary

This chapter reviewed the key methods and materials that were used to characterize a 2D granular memristive sensor. These topics form the foundation used to describe what is seen during the experiments that will be outlined in Chapter IV. Memristive characteristics and abundance of copper species present in the spheres can be used to predict the ideal material configuration needed for specific sensor requirements.

III. Methodology

The purpose of this chapter is to explain the experimental processes that were used to produce and characterize the two-dimensional granular memristive sensor. The first section will address the copper spheres and the process used to grow the oxide layer needed to form the MIM structure. The second section will discuss the specifications of the test fixture and how it was modified to improve the quality of electrical contact. The third section will outline the test set-up used to gather the data analyzed in Chapter IV. The chapter will conclude with SEM, EDS, and XPS methods used to characterize the oxide surfaces in the three samples.

3.1 Copper Spheres

3.1.1 Manufacturers' Specifications

The copper spheres used in this study were purchased from *Industrial Tectonics Inc.* and manufactured by *Canfield Technologies* using a proprietary fabrication method [26]. According to the specifications, the sphere composition is oxygen free and a minimum of 99.95% copper. The remaining 0.05% was listed as silver. The size and tolerance of the spheres are summarized in Table 1.

Size	Tolerance μm
Diameter	± 5.08
Sphereocity	± 10.16
Finish	0.127

Table 1. Copper Sphere Specifications for 700 μm Spheres [26]

3.1.2 Copper Spheres Oxidation

The thermal oxidation was performed on the (as received) copper spheres without processing, such as etching. The copper spheres were annealed in a Vulcan 3-130 furnace in air at 100°C for 5, 15, and 30 minutes. After the annealing time was completed, the samples remained in the oven for a 15-minute cooling period before opening the oven door. After the box furnace door was opened, a second cooling period of 15 minutes occurred, before the spheres were removed. A Pyrex petri dish was used to contain the spheres, which allowed them to spread into a single mono-layer. The box furnace was agitated for five seconds every time one-fourth of the oxidation time passed to assist in a uniform oxide growth. This meant that for the five-minute oxidation, the box furnace was agitated every 75 seconds; for the 30-minute oxidation, the box oven was agitated every seven minutes and thirty seconds.

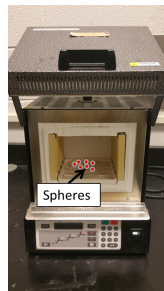


Figure 3.1. Illustration of sphere location in furnace during annealing

3.2 Test Fixture

3.2.1 Construction Materials

The test fixture base consisted of standard fiberglass used in Printed Circuit Board (PCB) construction and was built by *Journey Electronics*, based on specifications provided by Willey [8]. The contact material was SAC 305, which is a standard alloy also used in PCB construction. SAC 305 is 96.5% tin, 3% silver, and

0.5% copper. A DC bias was applied to spheres at specific locations using ribbon cables soldered to the pads on the PCB. Figure 3.2 contains photographs of the top and bottom of the first test fixture.

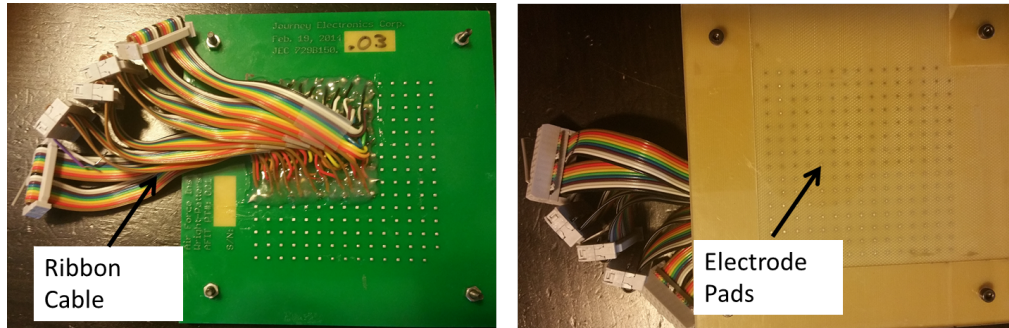


Figure 3.2. Test Fixture One: Above are pictures of the top and bottom the of first test fixture, which used pads as electrodes with DC bias being applied using ribbon cables soldered to the bottom.

The ribbon cables, which provided the means to make I-V measurements, were removed and replaced with tungsten pillars to provide better contact with the conductive filament formed during electroforming. Two sets of tungsten pillars, α and β , were placed perpendicular along the boundary of the test fixture, as shown in Figure 3.3. Each tungsten pillar was placed 5mm apart with both sets of tungsten pillars sharing a node at the connecting corner. The tungsten pillars were identified using Cartesian coordinates with the shared electrode being labeled, $(0,a)$, when I-V measurement is along the α set of electrodes, and labeled, $(b,0)$, when along the β set of electrodes. The ground electrode is located at $(2,2)$ and is 10mm from both electrode $(0,2)$ and $(2,0)$.

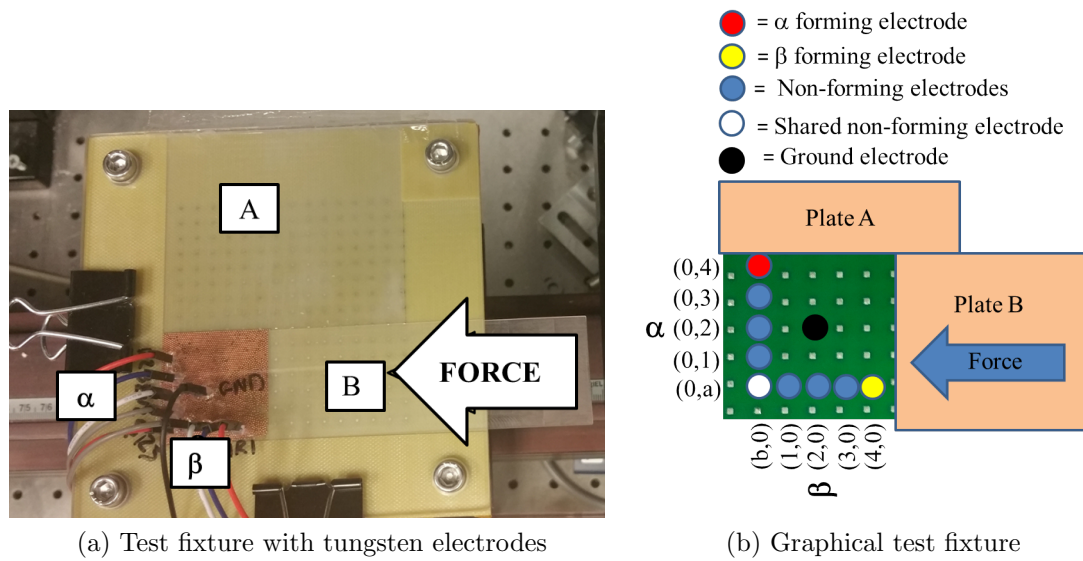


Figure 3.3. Physical and graphical representations of the second test fixture

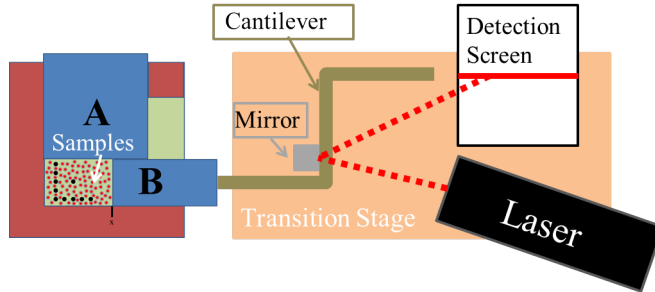
Plastic plates were milled to fit the 748mm x 0.746mm test fixture openings located at the boundaries opposite the tungsten electrodes. The plates provided the walls that defined the sphere plane area. Plate A is 748mm x 0.746mm x 95mm and provided the wall parallel to the β set of electrodes. Plate B is 35mm x 0.746mm x 95mm and provided the wall parallel to the α set of electrodes. Plate B was also used to apply the force during experiments discussed in the next section.

3.3 Experimental Set-Up

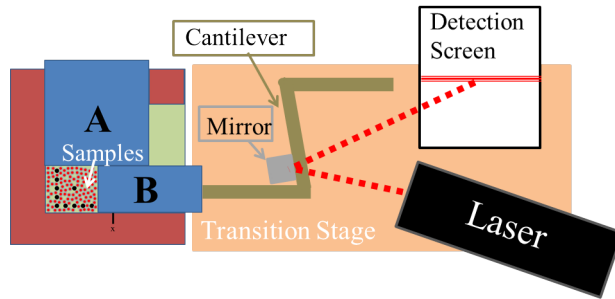
3.3.1 Test Fixture Set-Up

Figure 3.4 contains graphical, (a) (b), and physical, (c), depictions of the test set-up. The test fixture was mounted onto a stationary staging platform using risers, which were built at the AFIT machine shop. The Aerotech 130-XY computer-controlled micro-manipulator was used as a separate transition stage. A cantilever was mounted onto the transition stage to determine the amount of force being applied to the spheres. A mirror, mounted to the cantilever, and laser,

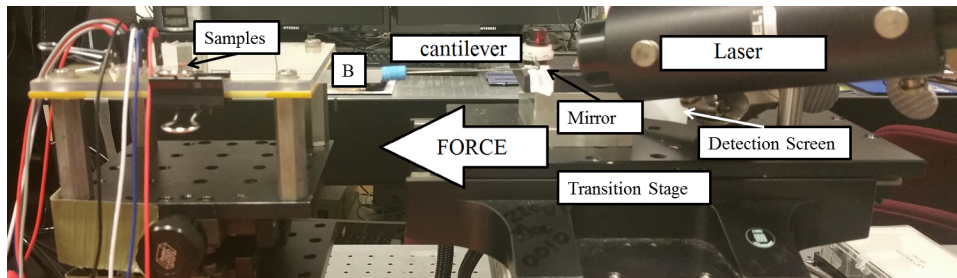
mounted on the transition stage, were used to detect the initial force. The method used to approximate the force applied to the spheres will be addressed in the next subsection.



(a) Test Fixture Pre-initial Force



(b) Test Fixture Post-initial Force



(c)

Figure 3.4. Experimental set-up with all major components labeled

3.3.2 Force Application

In order to approximate the force being applied to the spheres, a simple cantilever beam was constructed from tungsten with a pushing rod and mirror connected at one end. The other end was fixed. The transition stage was manually

adjusted until the cantilever was in contact with Plate B, Figure 3.4a. Next, the transition stage was advanced using computer controls until the cantilever first deflected, Figure 3.4b. This deflection was indicated by the laser on the detection screen changing, which indicated that a force was being applied. Deflection was considered to be 100% of the Aerotech ANT 130-XY movement after being initialized. The force at the end of the beam was calculated using Equation 8 [27].

$$F = \frac{3EI\delta}{l^3} \quad (8)$$

Where E is the Elastic Modulus of the beam in Pascal's, δ is the deflection of the beam in meters, l is the length of the beam in meters, and I is the second moment of inertia in $meters^4$ given by Equation 9.

$$I = \frac{\pi d^4}{64} \quad (9)$$

Where d in Equation 9 is the diameter of the cylindrical beam in meters. The characteristics of the tungsten beam used in this research are listed in Table 2.

Characteristic of Tungsten Cantilever	Value
Diameter (d)	$635\mu m$
Length (l)	$35mm$
Youngs Modulus	$400GPa$

Table 2. Characteristics of the tungsten cantilever used in this research.

3.4 Force Chains and Conductive Filaments

This section will provide descriptions of the possible scenarios that form memristive force chains when applying force to the two-dimensional copper memristive array. Understanding how conductive filaments were formed in the memristive force chains sets the stage for analyzing the data in Chapter IV. Figure

3.5 is a graphical representation of how the initial force chains were formed. Plate B was adjusted, using the method described in Section 3.3.2, until the spheres just begin to compress. Once the initial force chains were created, the spheres were electroformed using a 200V ramp and limiting current of $1\mu A$. The limiting current ensured the oxide layer did not completely break down as described in Section 2.2.1.

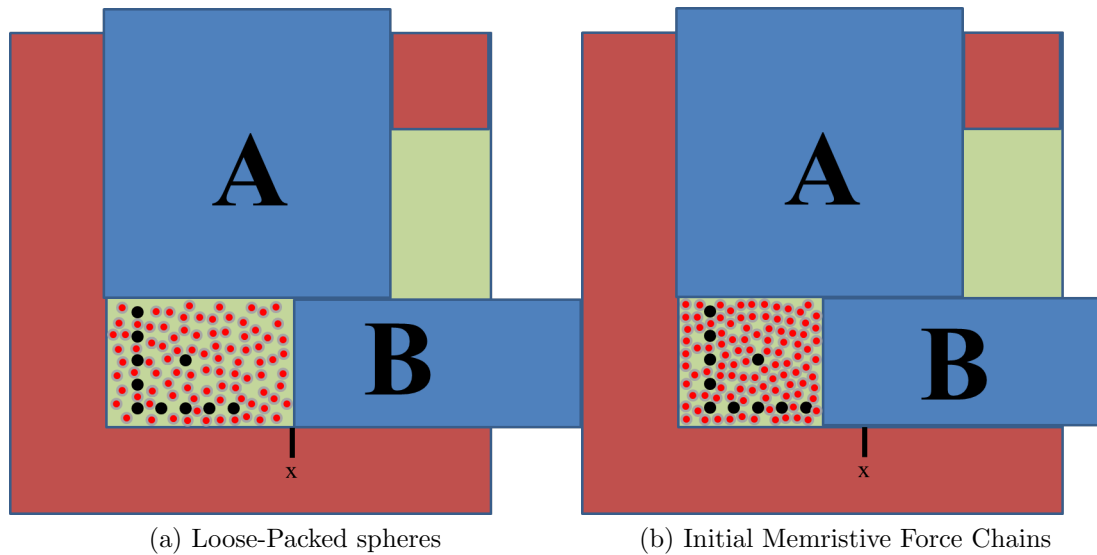


Figure 3.5. Forming Memristive Force Chains

During the electroforming process, conductive paths were created when pure copper filaments formed between spheres, due to soft breakdown of the oxide film. The formation of the conductive filaments was facilitated by the electric field and was speculated to occur due to a Mott transition, or redox reaction [28, 29]. A Mott transition is an insulator to conductor phase transition that occurs in some materials called Mott insulators. The transition is triggered when enough energy is added to the system to change the lattice constant to a critical length [30]. The redox reaction is thought of as nucleation growth process at the contact interface assisted by Joule heating increasing the mobility of oxygen ions which percolate off and create vacancies [28]. The copper ions reacted with the electrons left behind by

the oxygen and formed the conductive filament.

The copper filament can be represented as a tube of radius, r , length, l , and resistance, R , and electrical resistivity, ρ , using Equation 10 [19]. It can be noted that resistance of the wire will decrease as the cross-sectional area of the wire becomes larger.

$$R = \rho \frac{l}{\pi r^2} \quad (10)$$

Using this model, coupled with the concept of homogeneous nucleation and diffusion discussed in Section 2.3, a model was built to describe how the copper filament developed with subsequent voltage loops post forming. As the voltage loop was ramping up, so was the temperature in the filament due to Joule heating. Joule's First Law is

$$Q \propto i^2 R t \quad (11)$$

where Q was the amount of heat released, i was the current of the system, and t time. Equation 11 was combined with the equation for heat capacity, C_p , at constant pressure

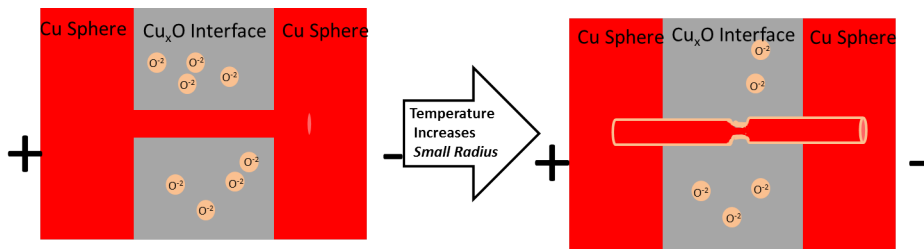
$$C_p = \frac{Q}{\Delta T} \quad (12)$$

to obtain a relationship between current, resistance, and temperature

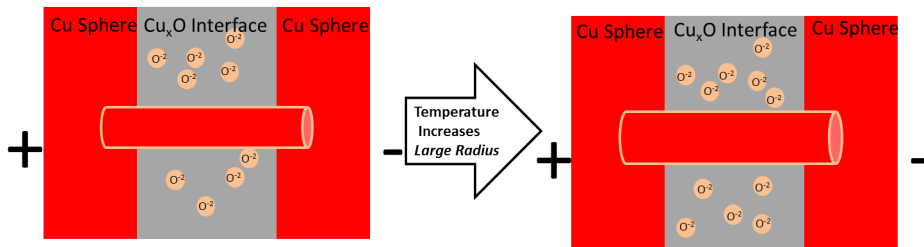
$$\Delta T = \frac{R i^2 t}{C_p} \quad (13)$$

Using Equation 10 and Equation 13, if the filament radius is small, the resistance will be high, and the temperature of the oxide surrounding the filament will be high. The high temperature will facilitate the diffusion of oxygen into the copper filament –pinching the filament closed as illustrated in Figure 3.6a. If the radius of the filament is large, the resistance of the filament will be small, and

current would be the controlling factor in the temperature change. Instead of oxidation reducing the filament size, the field effect, which occurred during electroforming, could continue and over power the oxidation. The field effect would allow the filament growth to stabilize as seen in Figure 3.6b. There would be a critical filament size which could be considered as a steady state. In the case, of the steady state, the oxide coating would be sufficiently thick enough to reduce the diffusion rate to an infinity-like state. In this case the filament would not increase or decrease but maintain a constant resistance over time.



(a) This graphic shows the copper filament shrinking due to diffusion of oxygen



(b) This graphic shows the copper filament growing due to copper lattice increasing from the field effect

Figure 3.6. Copper filament growth due to radius size

Another way the conductive filaments may be affected is through physical manipulation. If a large enough sheering force is applied, the conductive filaments in the structure will either decrease or increase in conductivity. The increase of conductivity would be caused by the surface area at their contact points increasing as in figure 3.7b, The decrease in conductivity would be due to the force being applied breaking the conductive filament, as well as the force chain collapsing as in

Figure 3.7a.

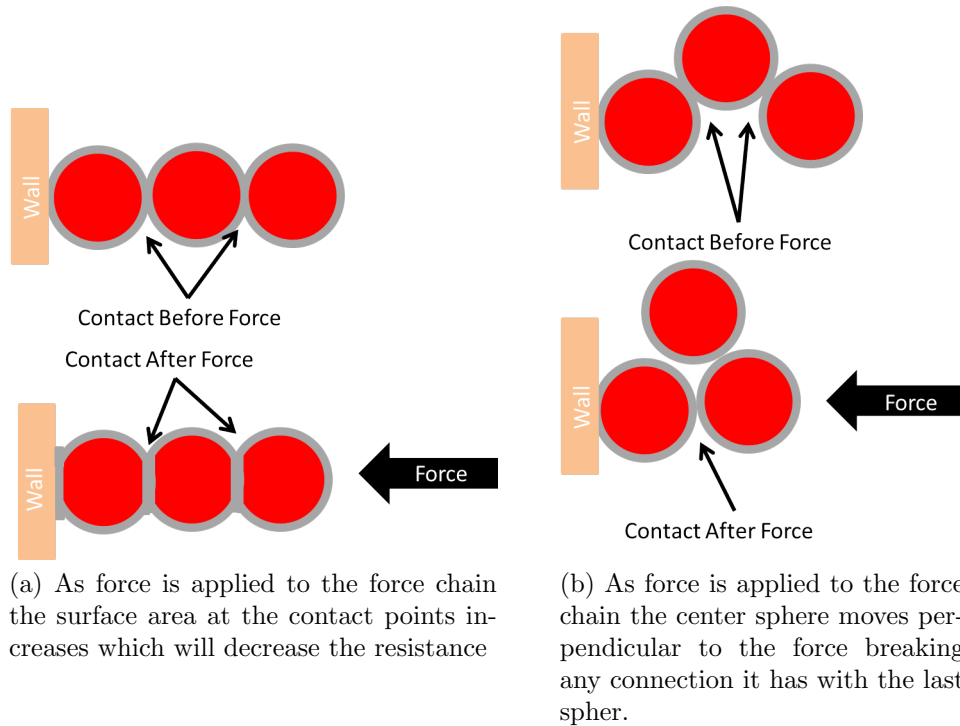


Figure 3.7. Force effects on conductive filaments

3.4.1 Scanning Electron Microscopy (SEM)

The Hitachi S-4700 SEM was used to examine the physical surfaces of the annealed copper spheres. SEM uses a focused beam of electrons to raster the material surface. The electron beam is focused using electromagnetic lenses and a final condenser lens to focus the electron beam down to the nanometer scale [31]. As the high-energy electrons, 30keV was used in this research, penetrate the material, they produce either backscattered electrons (BSEs) from elastic scattering or secondary electrons (SEs) from inelastic scattering. The BSEs and SEs are collected using two detectors. A Faraday cage is used to select the SEs, while the BSEs detector is on the cone of the electron gun. After entering the detector, the electrons are converted to photons using a scintillator disk. The photons are then

displayed onto a screen after being amplified $10^6\times$. SEs provide the topographic contrast, while BSEs provide contrast in the elemental composition [31].

3.4.2 Energy Dispersive X-ray Spectroscopy (EDS)

The elemental composition of the copper spheres was measured via EDS using an Oxford Instruments 7200 Link Pentafet EDS X-Ray Detector. During electron bombardment of a material core electrons are ejected [31]. This atom will return to the ground state after an electron in an outer shell fills the vacancy left by the ejected electron. As the outer shell electrons falls to fill the inner electron shell, the energy difference of the shells is given off as either a characteristic X-ray or Auger electron. In EDS, the characteristic X-rays are detected using p-type silicon and lithium diode (Si(Li)). The Si(Li) generates electron-hole pairs based on the energy of the X-ray. The higher the X-ray energy, the more electron-hole pairs generated, which are converted to an electric charge. The difference in charge values can be used to create the EDS spectrum represented as the intensity of characteristic X-ray lines across the X-ray energy range [31].

3.4.3 XPS Measurement Method

The spheres were mounted onto a tantalum disk, using silver paste, for XPS analysis, and may be seen in Figure 3.8. The samples were measured under ultra-high vacuum conditions (10^{-9} Torr). A XR 50/XRC 50 HQ x-ray source was used to measure $Cu2p$ binding energies and $Cu2p$ Auger binding energies with a non-monochromatic Aluminum $K\alpha_1$ (1486.61eV) source. A Keithly 2200-60-2 programmable power supply was used to actively bias the sample to zero potential in relation to the electron analyzer. Photoelectrons were detected by a hemispherical analyzer with a $\frac{0.8}{2.5548}$ eV resolution. The system's work function was

determined to be 4.35eV using a single gold crystal. The source power was set to 100W during the alignment process to reduce the chance of CuO to Cu_2O reduction, which will be discussed in Chapter 4.1.3.



Figure 3.8. The picture shows the copper spheres, which were annealed for 15 Min, mounted in silver paste for XPS analysis.

3.5 Summary

Chapter 3 explained the material processing, experimental set-up, and characterization techniques used to study the two-dimensional granular memristive sensor. The chapter started with a detailed explanation of the thermal oxidation process used to create the spherical samples. The oxidation process was followed by the test fixture development and set-up. The force measurement method, filament formation, and filament growth were also discussed. Finally, the surface characterization methods used to investigate the copper spheres were covered. Chapter IV will present an analysis of the gathered data.

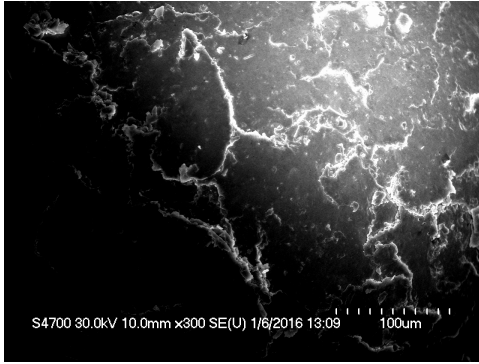
IV. Results and Analysis

This chapter will present the results from the research and provide data interpretation. The researcher will start by comparing the oxide coating composition for the three samples created by evaluating SEM, EDS, and XPS data. Following the oxide coating composition, the process used to implement the main electrical test will be explained for clarification. Finally, the chapter will examine the data gathered on the three samples.

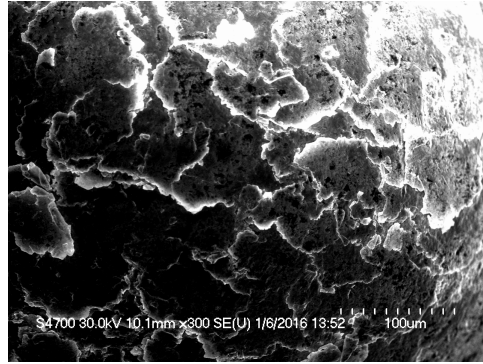
4.1 Oxide Composition

4.1.1 SEM Images

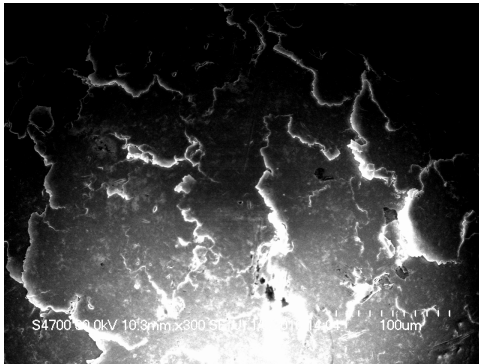
Figure 4.1 shows 300x SEM photos taken of the untreated spheres, 5-min annealed spheres, and 15-min annealed spheres. The surface of all the samples looks similarly rough and flaky. There is a charging effect taking place at the edge of the cracks in the oxide, which was indicative of an insulator. It appeared as if the charging effect increases with annealing time indicating a thicker oxide film is present.



(a) SEM 300x Untreated



(b) SEM 300x 5 Minute



(c) SEM 300x 15 Minute

Figure 4.1. SEM data for annealed spheres

4.1.2 Energy Dispersive X-ray Spectroscopy

While the surface images of the spheres were being taken, EDS was used to measure the %wt of oxygen and copper on the surface. Table 3 lists the results in %At, which should be 50/50 Oxygen and Copper, if the area being sampled contains only copper oxides.

Specimen	%At O	%At Cu
Untreated	10.27	89.73
5 Minute	8.69	91.31
15 Minute	12.13	87.87
30 Minute	11.27	88.73

Table 3. EDS Data of Copper Spheres

This was not the case, however, and all four samples indicated a 10% Oxygen 90% Copper stoichiometry. The large difference from the expected value was due to the small thickness of the oxide layer, which was estimated to be 5-10nm by Orta [1]. This thin layer would only contribute a small amount of the characteristic X-rays, which can escape from as deep as $2\mu\text{m}$. The majority of the characteristic X-rays would have come from deeper in the sphere and were considered to be pure copper. Figure 4.2 shows a typical SEM interaction volume of signal events.

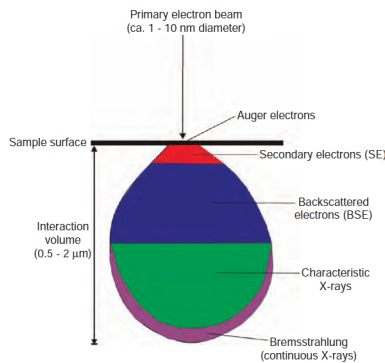
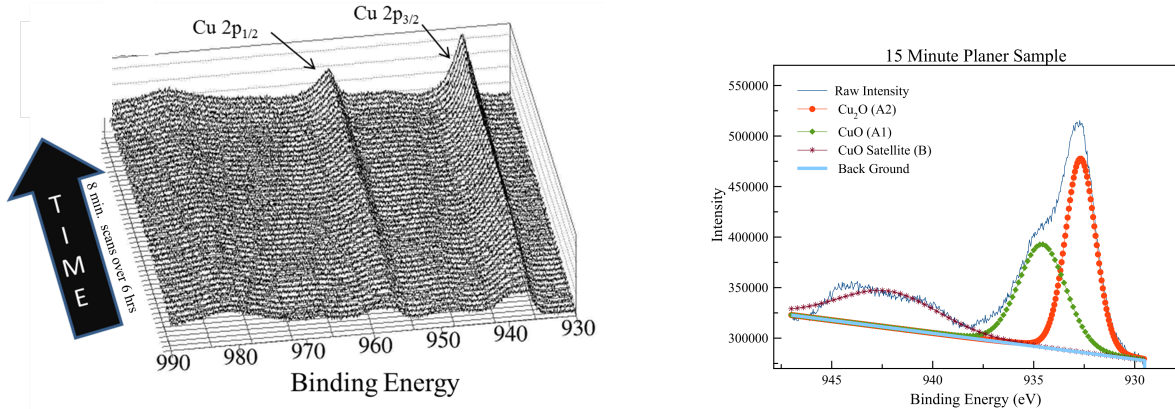


Figure 4.2. This graphic indicates the area and depth of the signal events that occur during SEM measurements. The characteristic X-rays can come from as deep as $2\mu\text{m}$, which makes EDS a poor choice when studying thin films, such as those grown on the copper spheres in this study.

4.1.3 CuO to Cu_xO Reduction

Figure 4.3 shows XPS spectrum of the copper 2p region for planar samples that were oxidized by Castle for 15 minutes in a 50/50 Argon/Oxygen environment [25]. The data to create the plots were collected at different times from similar samples. Figure 4.3b shows the $\text{Cu}2p_{3/2}$ region of the copper spectrum with the copper species represented by peaks: A1 (Cu_2O), A2 (CuO), and B (CuO satellite peak). Figure 4.3a is a three-dimensional plot of the entire copper 2p spectrum taken in eight-minute intervals over a six-hour period. It is clear that CuO (A2), represented by the strong shoulder centered around 935eV , was being reduced to Cu_2O (A1) as

peak A2 decreased while peak A1 increased over the six-hour period. In order to avoid this reduction impacting the spectrum of the sphere samples, each scan was limited to 30 minutes.



(a) Copper XPS spectrum scanned every eight minutes for 6 hours. The reduction of CuO to Cu_2O may be seen as the shoulder centered at $935eV$ decreases as the main peak at $932eV$ increases. Plot provided by Dr. Tony Kelly.

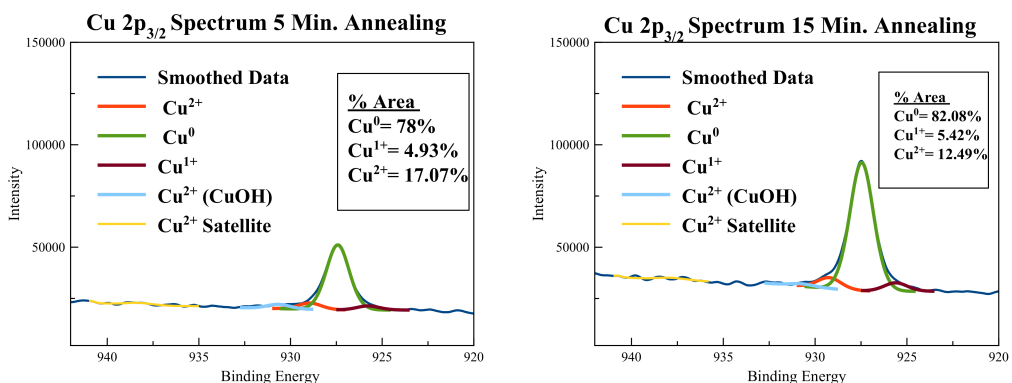
(b) The $2p_{3/2}$ region of the copper XPS spectrum of 15-minute planar sample annealed in 50% argon 50% oxygen mixture.

Figure 4.3. These plots show that a reduction of CuO to Cu_2O occurs when copper oxide is exposed to X-rays for extended periods of time.

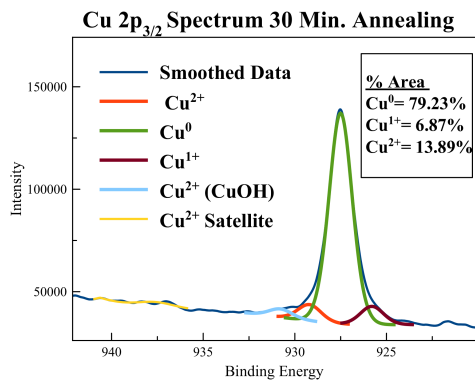
4.1.4 Oxide Composition via XPS

Samples of copper spheres were prepared for XPS analysis to compare how the oxide growth varied with oxidation time. The changes in the surface condition could be used to model the characteristics of the memristive granular system and assist with determining material need to fulfill user requirements. Figure 4.4 shows the $Cu2p_{3/2}$ spectrum for the three samples. *Casa* software was used to fit the 30-minute sample spectrum; then, the fitting parameters were cascaded to the 15-minute and 5-minute samples.

The intensities of each sample varied greatly. This could be due to the lack of sample shape in the mounted copper spheres. The spheres were mounted, by hand, onto tantalum disks using silver paste. The density of spheres, sample shape, and



(a) $Cu2p_{3/2}$ spectrum from the 5-minute sample (b) $Cu2p_{3/2}$ spectrum from the 15-minute sample



(c) $Cu2p_{3/2}$ spectrum from the 30-minute sample

Figure 4.4. This figure shows the $Cu2p_{3/2}$ XPS spectrum for the (a) 5-minute sample (b) 15-minute sample (c) 30-minute sample. The intensities vary; however, the percentage area implies that the three samples' thickness variations were a smaller scale than the overall thickness.

sample size all varied. Alignment of the X-ray beam could have contributed to the difference in intensity values from sample to sample.

Although the intensity counts vary significantly, the percentage area of each copper species are similar: $Cu^0 \pm 2\%$, $Cu^{1+} \pm 1\%$, and $Cu^{2+} \pm 3\%$. All three samples appeared to have an oxide film in which the variation in thickness is a smaller scale than the overall thickness. Also, the lack of a strong shoulder showing the presence of CuO indicated the oxide layer was much thinner than on the planar samples discussed in Section 4.1.3. The similarity in oxide coating thickness is thought to be due to a native oxide present on the samples before annealing. If the oxide coating were equal to a critical thickness, the oxygen would need more time to diffuse through the native oxide and increase the thickness.

There was a static charge on the surface, which indicates that an oxide film was formed during annealing. Section 2.4.3 addressed the binding energies of the different copper species; it specifically stated that Cu^0 has a binding energy of $932.61 \pm 0.025eV$ [23]. However, the spectra measured in this study were centered at $927.46 \pm 0.04eV$ for the three samples. This static charge could also be seen physically, in Figure 4.6, when the copper spheres would adhere to the sides of their containers after being annealed. The shift in the spectra were thought to be due to the photoelectrons leaving at a higher rate than they could be replaced by the power supply discussed in Section 3.4.3. Figure 4.5 shows the normalized envelopes of the $Cu2p_{3/2}$ XPS spectra for the three samples, along with a line, which indicates the standard location of the $Cu2p_{3/2}$ peak according to Biesinger [23].

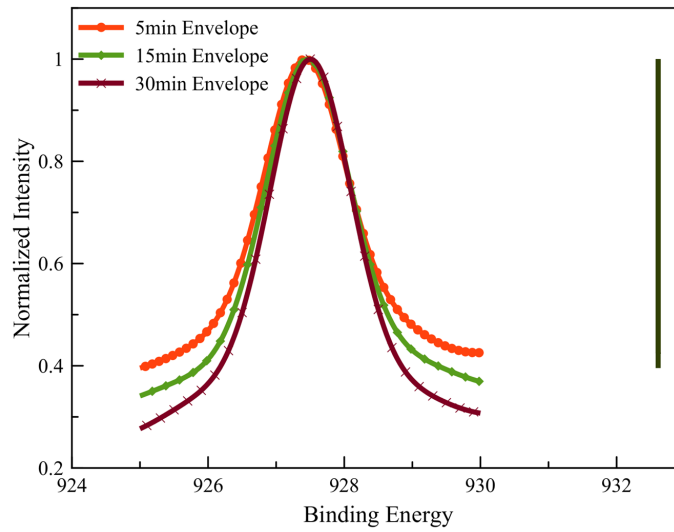


Figure 4.5. Normalize $Cu2p_{3/2}$ XPS Spectrums for 5-, 15-, and 30- min samples with line indicating standard location of envelope peak. This shift is thought to be due to photo electrons leaving at a higher rate than they could be replaced by the power supply actively biasing the samples.

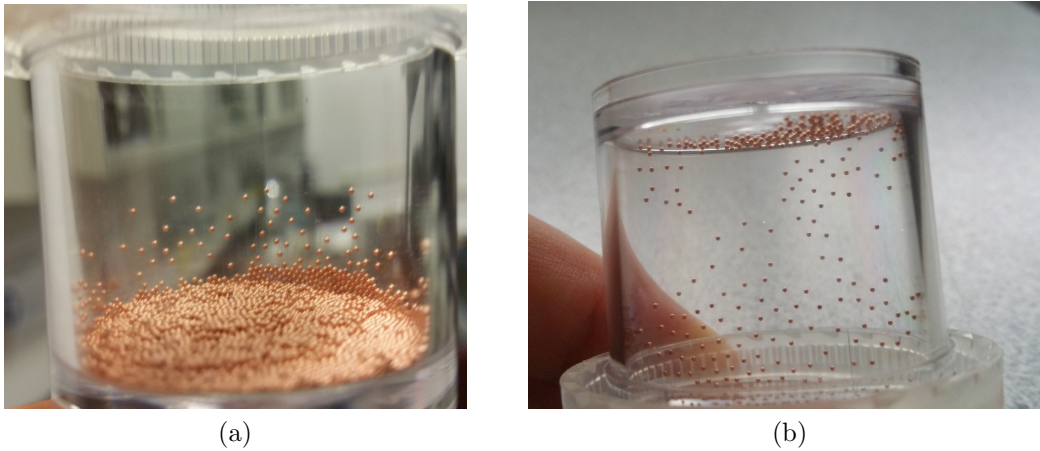


Figure 4.6. Floating spheres due to static charge on the copper oxide thin film

Due to all the collected data pointing to the oxide film scale thickness being a smaller scale than the film itself, two more samples were created using the process described in Section 3.1.2 using $200^{\circ}C$, but no analysis was conducted on them at the time of this writing. Figure 4.7a shows photos of the five minute sample used in this research, while Figures 4.7b and 4.7c are samples treated at $200^{\circ}C$ for

5-minutes and 30-minutes respectively. The red color seen in Figure 4.7b is indicative for the presence of Cu_2O . The inhomogeneity of the samples annealed at $200^\circ C$ was caused by the temperature being larger near the Pyrex dish walls. When the dish was removed, the spheres touching the dish wall were purple, which is indicative of a thicker coating of Cu_2O .

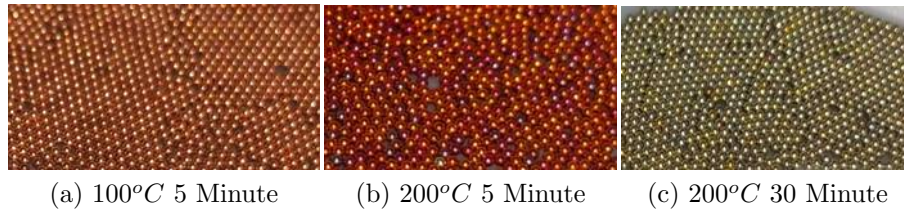


Figure 4.7. (a) shows the spheres that were annealed for five minutes at $100^\circ C$; the 15- and 30- minute samples had a similar color and shine. (b) shows spheres that were annealed at $200^\circ C$ for five minutes. The red and purple color was indicative of the Cu_2O . (c) are spheres that were annealed at $200^\circ C$ for 30 minutes. The gold and silver color could be from the presence of a contaminate during annealing or a mixture of oxide species.

4.2 Initialization and Test Procedure

The initialization of the system and test procedure are included here rather than Chapter III to reacquaint the reader with the notation used for the test fixture. The test fixture base provided two of the walls necessary to confine the sphere samples. Along each of these walls was a set of five tungsten electrodes referred to as α and β . The tungsten electrodes were labeled using Cartesian coordinates with the (0,0) position being shared by both α and β , as can be seen in Figure 4.8. The ground electrode was located at coordinates (2,2) and was used for all measurements. Plate A and Plate B provided the remaining walls to confine the spheres for testing. Plate A remained stationary for all measurements, while Plate B was advanced by the cantilever and transition stage to apply forces. The initialization procedure for all test performed with the test fixture was as follows.

1. The transition stage and *Plate B* were manually adjusted until spheres were confined in the location of the tungsten electrodes with a visible gap, Figure 3.4a.
2. The transition stage was used to advance *Plate B* in 0.1mm steps until the cantilever deflected, Figure 3.4b.
3. The transition stage was reversed 0.1mm , and *Plate B* was adjusted to be in contact with the cantilever

The state of the system after step 3. was considered the initial position. The initial force is referred to as zero force, although it is reasonable to assume a small force may exist on the confined spheres.

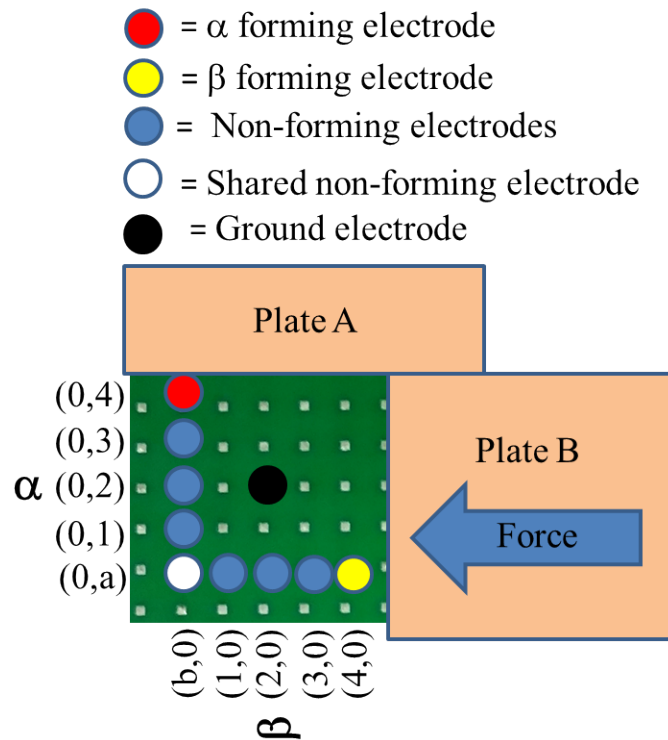


Figure 4.8. This graphic shows the location and Cartesian label for each node in the test fixture. The forming nodes are (0,4) for the α set of nodes and (4,0) for the β set of nodes. Node (0,0) is labeled differently depending on the node set being measured: (0,a) for α and (0,b) for β . All measurement sequences of nodes start at the forming node and progress toward node (0,0).

After initialization, the electroforming process was performed between ground and node (0,4) for α measurements, or between ground and node (4,0) for β measurements. Electroforming consisted of applying a 200V DC ramp with a limiting current of $100\mu A$. The limiting current ensured soft breakdown occurred, which allowed the conductive filaments to form. Post electroforming, force was either fixed or varied, from 0 to 220mN, in 22mN steps, and a 500mV bias ramp was applied to each node starting with the forming node and ending with node (0,0). The 500mV bias ramp consisted of the following: 0 V increasing to 500mV, 500mV decreasing to 0V, 0V decreasing to -500mV, and -500mV increasing to 0V.

If the force were fixed, time was used as the variable to observe how the conductive filaments reacted. A base value of $t = 30$ minutes was used with measurements taken at $0t$, $1t$, $2t$, $4t$, $6t$, $38t$, and $39t$. The 500mV bias was repeated three times for each time point. When force was varied, the transition stage was advanced 0.1mm, which is approximately $22mN$ using Equation 8. The 500mV bias was again applied to each node starting with the forming node and ending with node (0,0). This process was repeated for 0mm to 1.0mm, which is a total force range of 0 to 220mN. The following sections will discuss the various results from the two experiments.

Regardless of force being varied or held constant, the status of an electrode post electroforming was either ON or OFF. If the electrode were ON, it had a resistance between 0 and $600\ \Omega$. Figure 4.9a is an example of an ON electrode. If the electrode were OFF, then it had a resistance greater than $1M\Omega$. Figure 4.10f is representative of an OFF electrode. Figure 4.10f is also indicative of an I-V curve that is outside the 30 picoamp minimum specification current for the Keithly 4200-SCS, so the true resistance of the system is unknown. Whether the node was ON or OFF was random, as the forming path was not limited to any specific set of

spheres. Therefore, the data sets in this research show capabilities of the jammed granular memristive system, but many more data sets are need before a field able system can be created.

4.3 Constant Force Measurements

Figure 4.9 illustrates all of the I-V plots for the forming node (0,4) in sequential order from 0t to 39t. The mean value is approximately 9.5Ω with a 6% error. This constant value demonstrated that, during the electroforming process, the filament that formed between ground and (0,4) had reached steady state as described in Section 3.4 and was unlikely to degrade over time. The stability of the forming node filament also showed a robustness to force, which will be described in the next section.

Figure 4.10 shows the I-V plots for node (0,3). From the measurement taken at 0t and 1t, it appears as if the filament's conductivity was on the path to steady state and the field effect was not allowing oxidation to dominate. However, the measurements at 2t indicated there must have been a conductive filament that had not completely formed. The closing of the conductive path can be seen in cycle 1 of the 2t α measurement, as the resistance started off at $\approx 100\Omega$, which was double the two previous measurement sets. The increase in resistances caused the temperature in the surrounding oxide to increase, which allowed the abundance of oxygen present at the surface to flood in at $400mA$. This oxidation further increased the resistance and pinched off the conductive path. The resistance continued to increase during cycle 2 and cycle 3 until the diffusion rate was decreased due to the oxide thickness. The oxidation continued while the electric field was not directly applied. At 4t, the conductive path is completely shut off. At 6t, the electroforming effect of the biasing voltage allowed (0,3) to turn on again at $10K\Omega$ during cycle 1 and decreased

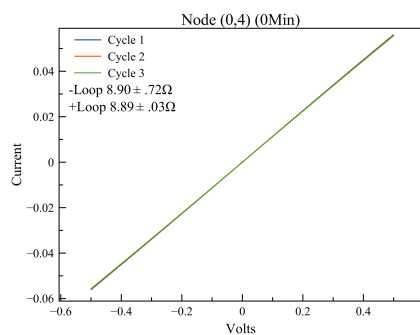
to $2K\Omega$ by the end of cycle 3. It was assumed that, if enough voltage loops were performed, the original 40Ω reading could be reached. However, the recovery was not significant enough to prevent the filament from closing again during 38t. The plot 39t shows signs of the field effect working to turn the filament back on, but this was an artifact of the test equipment. Similar I-V curves could be generated when test probes were not connected to any device.

Figure 4.11 shows the sequential plots for node (0,2), which was the middle node inline with ground. This filament was not able to complete its growth during electroforming. However, the oxide layer stopping the current was thin and was broken through a field-driven process, which allowed filament growth to complete the conduction path. The growth of the conductive filament was observed, when the channel turned on during cycle 3 of the 1t measurements. Although the resistance was reduced to 13Ω , indicating a strong connection, the thickness of the conductive filament must be extremely thin, which allowed oxidation to close the channel during the dwell time between 1t and 2t. The activity during 2t showed there was a fight to turn the channel back on. The oxide, which had shut off the channel during the 2t measurement, was again destroyed at the start of the 4t measurements. This on off battle between the conductive filament and oxide film continued with the conductive filament becoming stronger each time. This was indicated by the continued reduction in resistance each time the channel returned and also in the 38t and 39t measurement sets, when oxidation did not close the channel again.

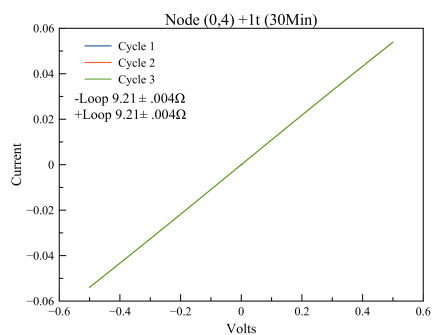
Figure 4.12 show the plots for electrode (0,1). A similar fight between diffusion of oxygen and filament growth, which occurred at (0,4), can be seen over the seven plots. The primary difference was that the strength of the conductive filament was only strong enough to remain open until the long dwell time between 6t and 38t. This set of figures illustrated that the electroforming effect occurs a significant

distance from the forming node.

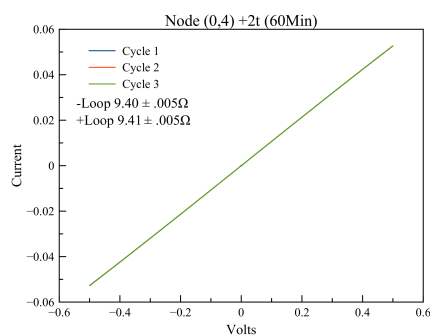
Finally, Figure 4.13 presents the plots for electrode (0,a). This node was furthest from the forming node, but the filament strength appeared to be strong, as the resistance decreased with each set of voltage loops. It is difficult to determine if the 38t measurement was due to diffusion or environmental affects such as vibrations. Regardless, the filament strength of (0,a) can be seen as it rebounds and continues to stabilize.



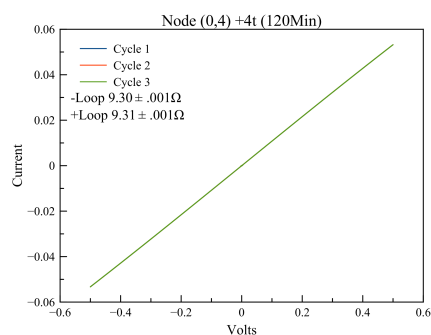
(a) 0t (0,4)



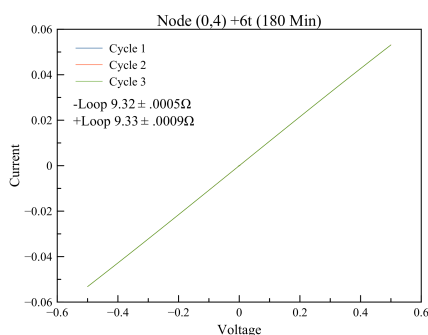
(b) 1t (0,4)



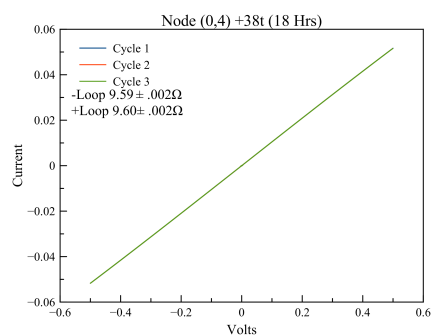
(c) 2t(0,4)



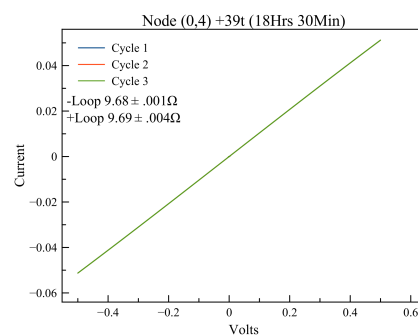
(d) 4t (0,4)



(e) 6t (0,4)



(f) 38t (0,4)



(g) 39t (0,4)

Figure 4.9. Electrode (0,4) I-V curves with constant force. This set of carts is indicative of a stable conductive filament. The change in resistance from 8.90Ω to 9.68Ω demonstrates that the field effect, which occurs during electroforming can counter the oxidation that is facilitated by the temperature increase in the oxide surrounding the filament.

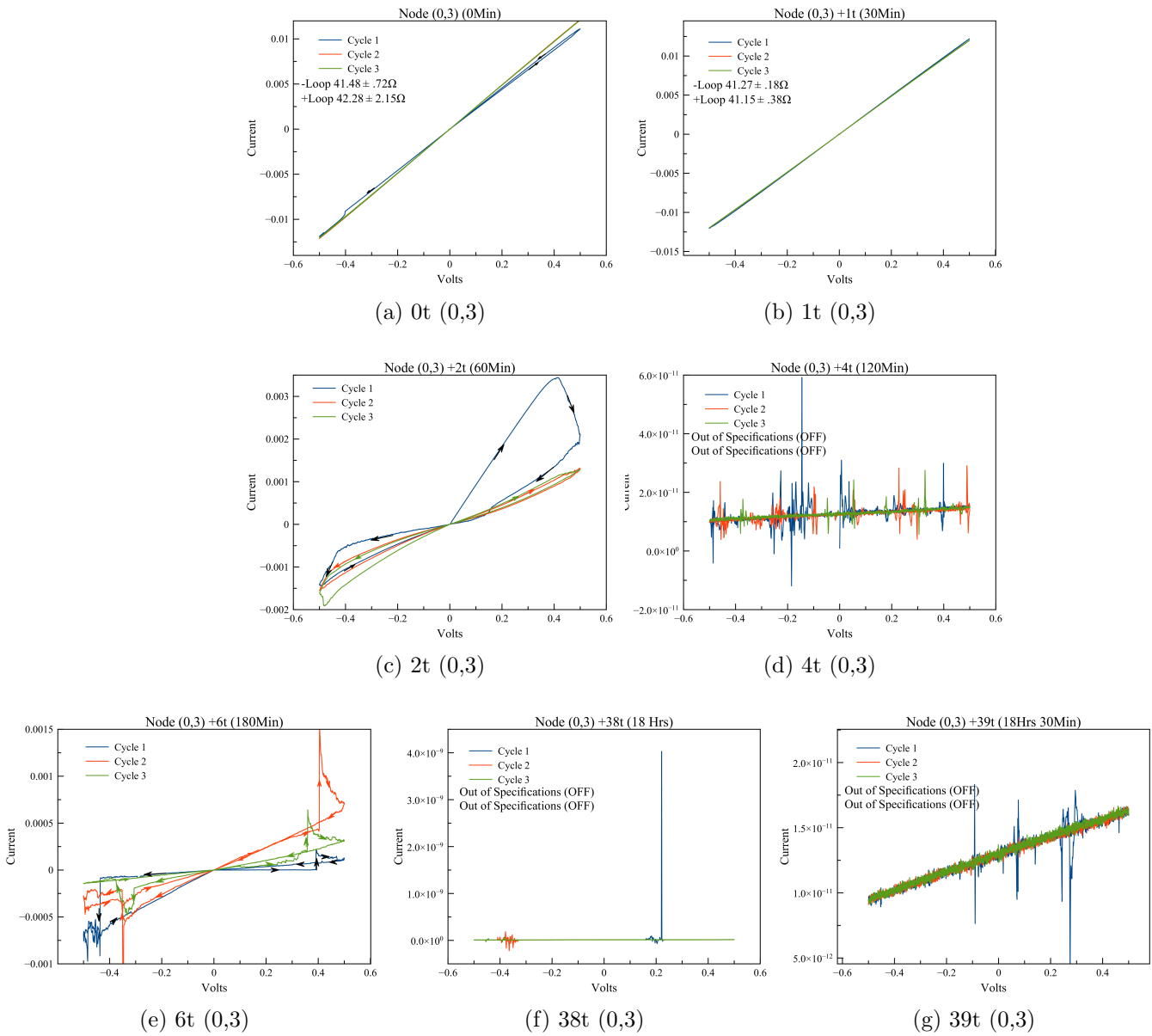
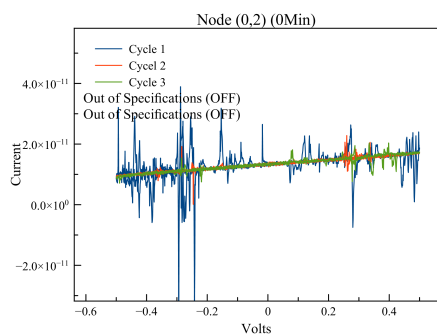
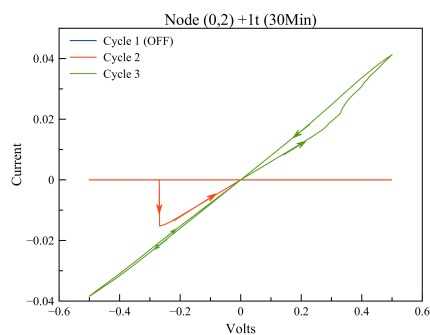


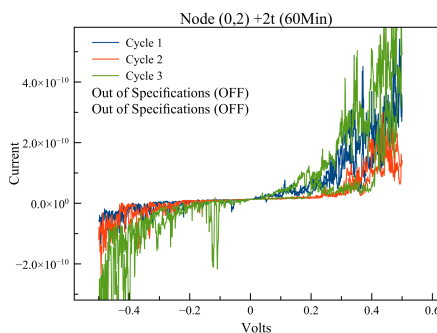
Figure 4.10. Electrode (0,3) I-V curves with constant force. This set of charts demonstrates how an unstable filament could react when lower-biasing voltages are applied post electroforming. It appears as if the filament is stable at 40Ω in (a) and (b), however oxidation is facilitated in (c) due to a resistance doubling during the dwell time between (b) and (c). The I-V curve in (d) is out of the specification range of the test equipment and shows the filament has been destroyed. (e) however, indicates that filaments can develop again without the need of repeating electroforming.



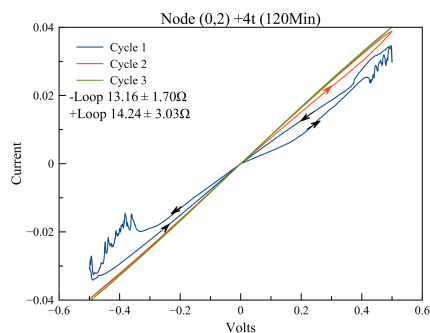
(a) 0t (0,2)



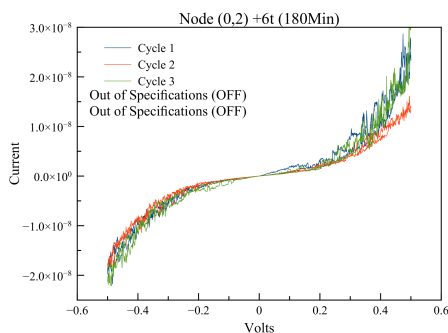
(b) 1t (0,2)



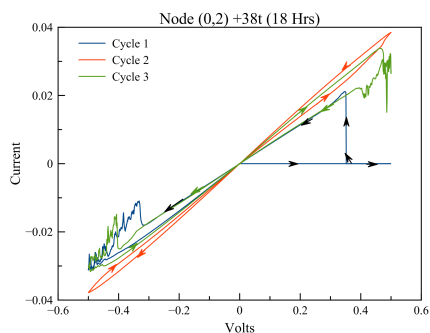
(c) 2t (0,2)



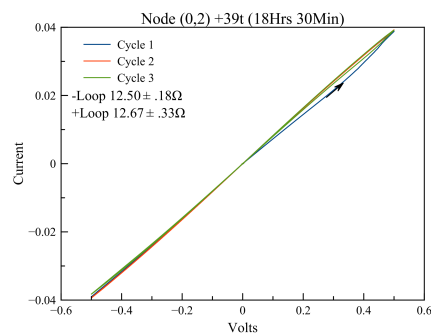
(d) 4t (0,2)



(e) 6t (0,2)

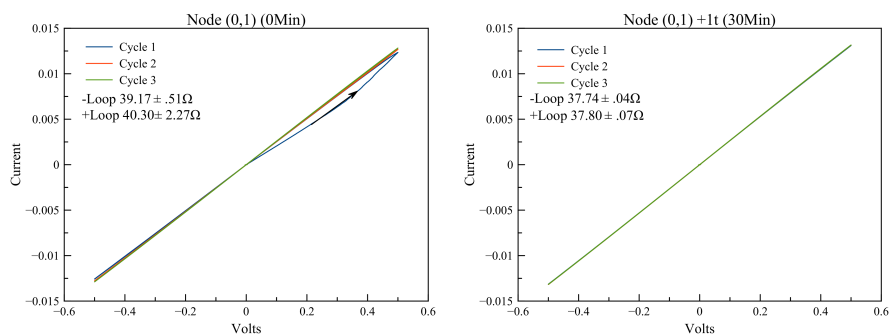


(f) 38t (0,2)



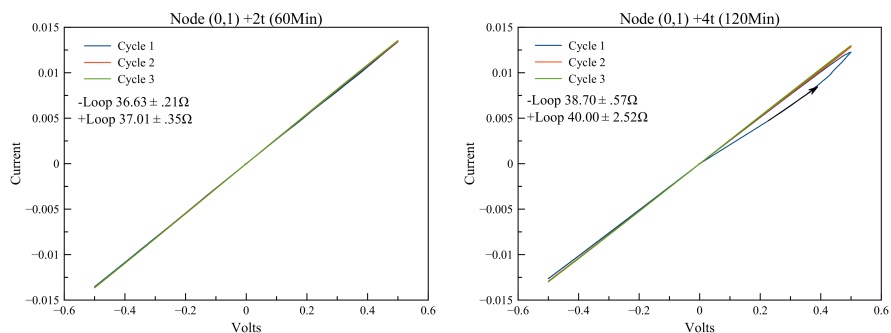
(g) 39t (0,2)

Figure 4.11. Electrode (0,2) I-V curves with constant force. This set of curves established that the conductive filaments do not need to be formed during the electroforming process. The I-V curve in (a) was clearly off and remains off until cycle 2 of (b) when resistance dropped to approximately 13Ω . The fight between oxidation during the dwell times and the continuation of the field effect that began during electroforming, can be seen in (c) through (g) as the conductive filament turns on and off.



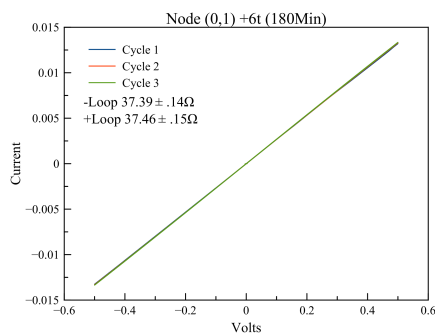
(a) 0t (0,1)

(b) 1t (0,1)

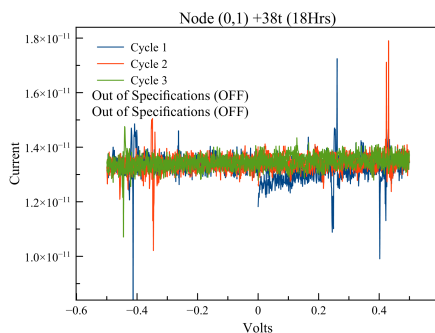


(c) 2t (0,1)

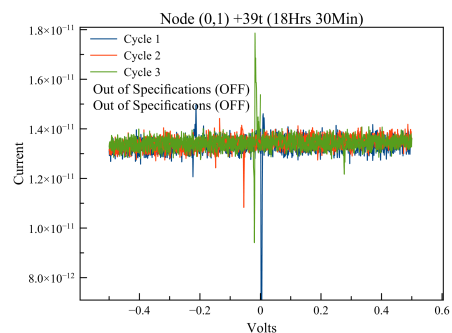
(d) 4t (0,1)



(e) 6t (0,1)

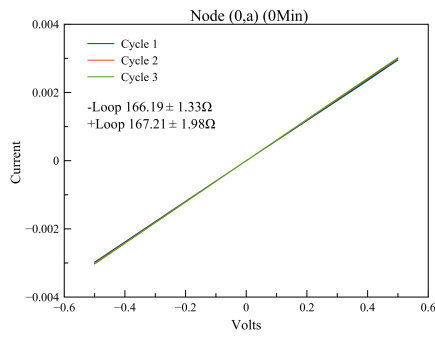


(f) 38t (0,1)

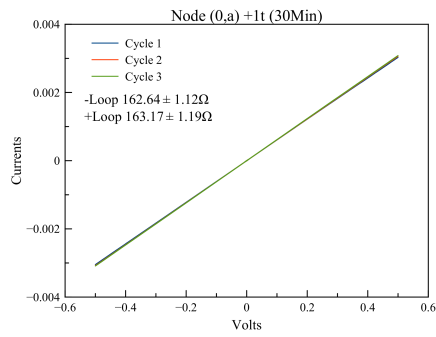


(g) 39t (0,1)

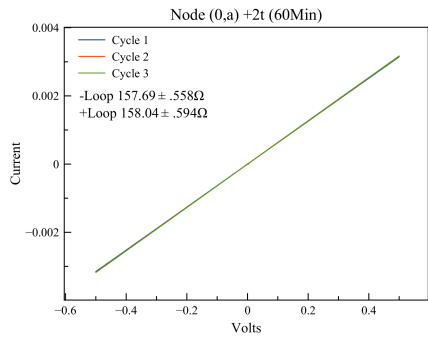
Figure 4.12. Electrode (0,1) I-V curves with constant force. I-V curves (a) through (e) exhibit the fact that stable filaments can be formed a significant distance away from the forming electrode. However, (f) and (g) demonstrate that oxidation of an apparently stable filament is still possible over a long period of time.



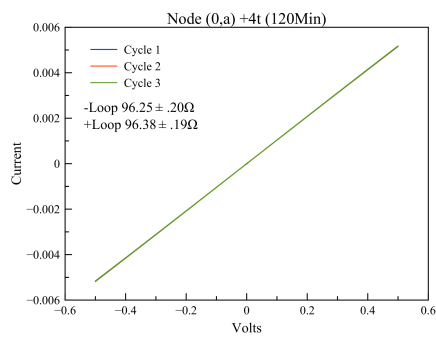
(a) 0t (0,a)



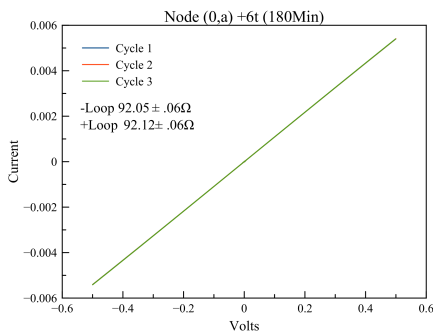
(b) 1t (0,a)



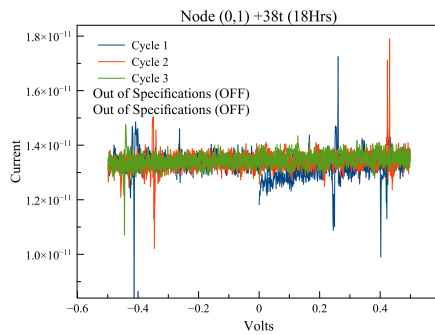
(c) 2t (0,a)



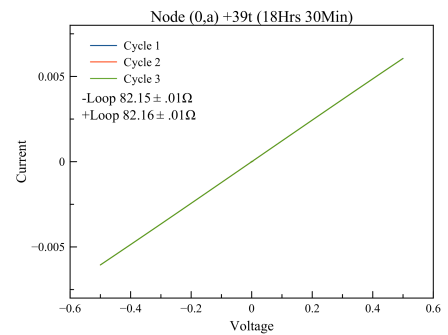
(d) 4t (0,a)



(e) 6t (0,a)



(f) 38t (0,a)



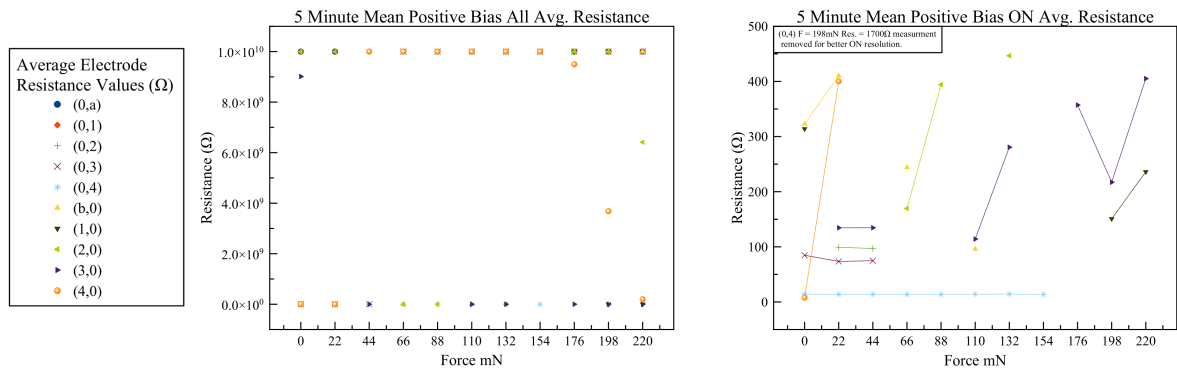
(g) 39t (0,a)

Figure 4.13. Electrode (0,a) I-V curves with constant force. This final set of I-V curves reinforces the ability of a stable filament forming a significant distance away from the forming electrode, with the capability of being turned off by oxidation and back on by the field effect.

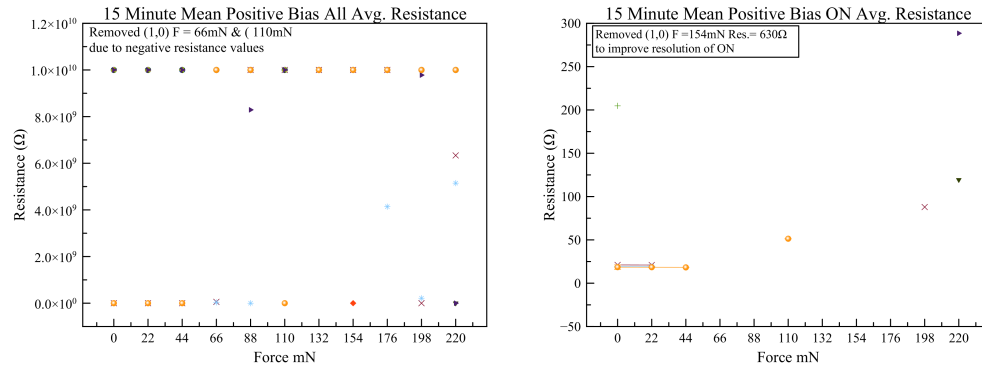
4.4 Varied Force Measurements

4.4.1 Resistance Over Large Force Steps (22mN)

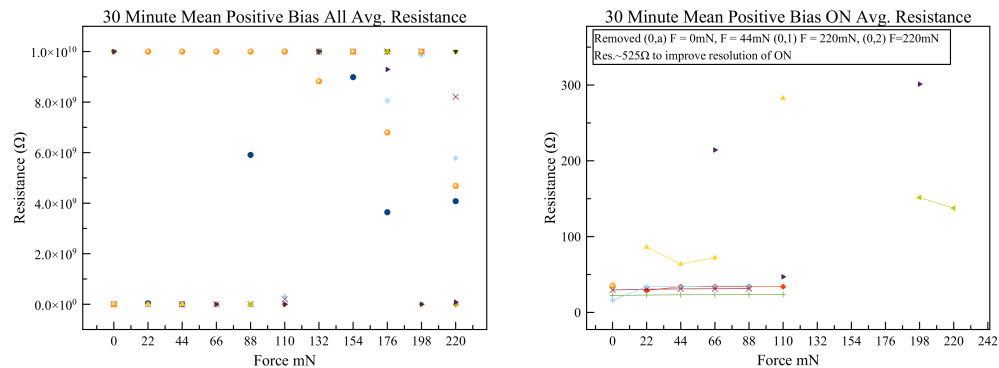
After comparing the I-V curves of the three samples over the change in force and not seeing any significant trends, the mean resistances were calculated and plotted in two sets –the positive loop values and the negative loop values. Figures 4.14b, 4.14d, and 4.14f shows the average resistance values of the positive bias portion post forming of the 500mV ramp. The majority of the values were in the $10^{10}\Omega$ range, in which the electrode was in an OFF state. Figures 4.14c, 4.14e, and 4.14g show only the nodes which were found in the ON state with lines connecting any subsequent on states. The resistance values for the ON electrodes fluctuated significantly; however, the forming electrode in line with the force for the five-minute and 30-minute annealed spheres does show robustness. The logic like fluctuation is attributed to an inconsistent packing method before electroforming. Only the laser movement described in Section 3.3.1 was used to indicate initial packing of the spheres, which meant there was most likely large voids, which allowed packed spheres too much freedom of movement.



(a) Legend (b) 5-Minute Mean Positive Loop Values (c) 5-Minute Mean Positive ON Values
22mN Steps 22mN Steps



(d) 15-Minute Mean Positive Loop Values (e) 15-Minute Mean Positive ON Values
22mN Steps 22mN Steps



(f) 30-Minute Mean Positive Loop Values (g) 30-Minute Mean Positive ON Values
22mN Steps 22mN Steps

Figure 4.14. Figures (b) (d) and (f) are the average resistance values of the positive bias portion post-forming and all three figures showing an ON/OFF logic pattern, which is due to inconsistent packing process. Figures (c) (e) and (g) are the ON resistance, which are all less than 600 Ω . The connected readings indicate subsequent ON values, which represent robust filaments that are stable for a large force.

4.4.2 Resistance Over Small Force Steps (5.6mN)

After discovering that the packing method was inconsistent and caused a logic ON/OFF state, a final test was performed identical to the method described in Section 4.2, with one exception. Plate B was advanced in 0.025mm increments, which equated to a 5.6mN force instead of the 22mN force. Figure 4.15 is a plot of the average resistance for the negative portion of the 500mV ramp. The connected lines indicate a continuation of an ON state of electrodes as the force varies. Electrode (0,4) was robust and consistent, as seen in the large force step experiments. The resistance of electrode (0,3) decreased from 72Ω to 30Ω , as the force increased from $11mN$ to $101mN$, which could be attributed to a continuation of the field effect that occurred during electroforming. Electrode (0,2) had the greatest fluctuation as it turned ON and OFF several times. This change in electrode (0,2) was thought to be due to the affect of the ground node (2,2) which was in line with the electrode and influenced the movement of the spheres while force was increased.

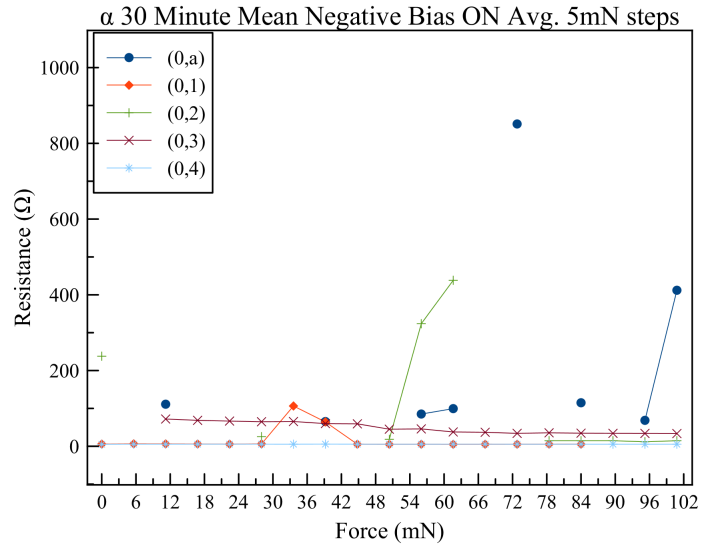


Figure 4.15. This chart shows how the life of the conductive filament is longer for smaller force steps. It is assumed that similar results would have occurred for large force steps, if the packing method had been more consistent. The significant fluctuation in electrode (0,2) measurements was thought to be caused by interference from the ground node (2,2), which was in line.

V. Conclusion

5.1 Overview

The goal of this research was to create a novel sensor that can detect intrusion via mechanical or electrical means using a jammed granular memristive system. This chapter will reflect on the data that were analyzed in Chapter IV and provide final thoughts on oxide growth and filament creation/destruction. A discussion of how these findings may be applied to a system protection technology will be given before closing the chapter with potential future work.

5.2 Oxide Growth

The similarity of the three $Cu2p_{3/2}$ spectra in Figure 4.4 shows that the change in the oxide thickness is insignificant when compared to their overall thickness. There was, however, a qualitative indication of Cu_2O growth, when the spheres were annealed at $200^\circ C$ for five minutes, Figure 4.7b. This change indicated that both time and temperature should be considered when growing oxide films of various thicknesses. The change in color of the sphere samples annealed for 30 minutes at $200^\circ C$, Figure 4.7c, may have been influenced by the presence of a contaminant. Plus, the inconsistent color in both 4.7b and 4.7c indicate that a more controlled oxidation method should be considered in the future.

5.3 Conductive Filament Formation

The field effect that occurred during electroforming caused soft break down and created the conductive filaments. The conductive filament path was not limited to the spheres between ground and the forming node. This can be seen by the decrease in resistance between ground and electrode (0,a) in Figure 4.13 and other

non-forming electrodes. The field effect continued to occur post electroforming when smaller biasing voltages are used as seen in Figure 4.11, when the electrode went from an OFF to ON state 30 minutes after electroforming occurred. Since the electric field has an affect across all spheres in the two dimensional sensor, a method to monitor all electrodes in real time is needed to gain a better understanding of the lifetime of a conductive filament.

5.4 Two-Dimensional Jammed Memristive Copper Sensor

The data analyzed in Chapter IV provide the building blocks to construct a two-dimensional jammed memristive copper sensor. In order for the sensor to be possible, there must be random initialization that the users can implement as their key. This randomness can be seen when comparing the first row in Table A.4. The sensor must also be able to detect electrical and physical manipulation. The detection of electrical manipulation was demonstrated in the constant force experiment. The growth and decay of the conductive filaments can be used as the variable of detection, which can be accomplished in multiple way.

1. Using the decay rate of the filament while interrogating the node at an incremental rate with a known resistance values. If an incorrect value is detected, time and manner for intrusion can be determined.
2. Applying a continuous bias voltage loop and monitoring resistance of the nodes at steady state. If electrical or physical intrusion occurs a profile of resistance change can be recorded in real time.
3. In a similar manner to 2, the granular material could be held without being electroformed at a known voltage and force. If manipulation occurs the resistance change across the node could be recorder to indicate what was

occurring and how.

The detection of mechanical manipulation was also seen in the variable force experiment. The inconsistent packing method showed a logic ON/OFF system. A more uniform packing method could provide a sensitivity control for detecting mechanical manipulation of the system, such that a loose packing would be more sensitive than tight packing.

5.5 Future Work

Due to the breath of research performed in this thesis, there are several paths open for future work. The electrical and mechanical properties of the copper spheres are well understood, but much can be done to develop a known consistent form. This may be accomplished by looking at the two samples not yet analyzed and adjusting the oxidation process temperature and timing. Using SEM with a larger magnification could help gain a better understanding of the spheres' topology, void and grain structure, which would assist with understanding the different contact scenarios that may occur between two spheres.

The fixed force experiment showed that the conductive filaments' stability can vary. If the filament is unstable, it can be destroyed by oxidation that is facilitated by the temperature increase in the surrounding oxide. This experiment could also be performed in an inert gas environment to have a better understanding of filament growth and decay.

The test fixture used to gather the I-V curves can be further developed by finding a method of filling that is consistent. Also the test fixture can be modified to measure the force change along the α wall to detect how much of the force is making it across the spheres. Finally, a method to apply force simultaneously in the α and β direction should be explored.

The measurement method of the I-V curves could be automated, which would make the acquisition of data faster. If a significant amount of data can be gathered in a short period of time, it could be used to build a reliable model to build fieldable sensors. A method to simultaneously capture I-V curve would also be beneficial. Filament growth is known to occur outside of the conductive path when the bias voltage is applied. By monitoring all the nodes simultaneously during biasing voltage loops, a better understanding of filament growth and decay may be discovered.

Appendix A. Logic Tables of Varied Force Measurements 22mN steps

Table A.4 shows the ON and OFF states of the measurements using a logic format with 1 representing a measurement below 600Ω and 0 representing a measurement above 600Ω . Using this logic chart, coupled with the mean resistance plots in Figure 4.14, one can begin to speculate how the conductive filaments were affected by the force. Similar to the constant force measure presented in Section ??, node (0,4) forms the most robust filaments. Similar statements cannot be made for electrode (4,0), the forming electrode perpendicular to the force.

All the surface analysis data support the oxide coating on the three spheres set are almost identical, and yet the on off spectrum of each measurement varied greatly. This was thought to be caused by the difference in sphere amounts loaded into the test fixture. If the 5-minute sample had significantly fewer spheres loaded than the 30-minute sample, the void area would be larger –allowing for the sphere to shift a greater amount and destroy the conductive filaments easier. A consistent loading method should be developed in the future.

Force (mN)	(0,a)	(0,1)	(0,2)	(0,3)	(0,4)	(b,0)	(1,0)	(2,0)	(3,0)	(4,0)
0	0	0	0	1	1	1	1	0	1	1
22	0	0	1	1	1	1	0	1	1	1
44	0	0	1	1	1	0	0	0	1	0
66	0	0	0	0	1	1	0	1	0	0
88	0	0	0	0	1	0	0	1	0	0
110	0	0	0	0	1	1	0	0	1	0
132	0	0	0	0	1	0	0	1	1	0
154	0	0	0	0	1	0	0	0	0	0
176	0	0	0	0	0	0	0	0	1	0
198	0	0	0	0	1	0	1	0	1	0
220	0	0	0	0	0	0	1	0	1	0

(a) 5 Minute Sample Logic Chart

Force (mN)	(0,a)	(0,1)	(0,2)	(0,3)	(0,4)	(b,0)	(1,0)	(2,0)	(3,0)	(4,0)
0	0	0	1	1	1	0	0	0	0	1
22	0	0	0	1	1	0	0	0	0	1
44	0	0	0	1	1	0	0	0	0	1
66	0	0	0	0	1	0	0	0	0	0
88	0	0	0	1	1	0	0	0	0	0
110	0	0	0	0	0	0	0	0	0	1
132	0	0	0	0	0	0	0	0	0	0
154	0	1	0	0	0	0	0	0	0	0
176	0	0	0	0	0	0	0	0	0	0
198	0	0	0	1	0	0	0	0	0	0
220	0	0	0	0	0	0	1	0	1	0

(b) 15 Minute Sample Logic Chart

Force (mN)	(0,a)	(0,1)	(0,2)	(0,3)	(0,4)	(b,0)	(1,0)	(2,0)	(3,0)	(4,0)
0	1	0	1	1	1	0	0	0	0	1
22	0	1	1	1	1	1	0	0	0	0
44	1	1	1	1	1	1	0	0	0	0
66	1	1	1	1	1	1	0	0	1	0
88	0	1	1	1	0	1	0	1	0	0
110	0	1	1	0	0	1	0	0	1	0
132	0	0	0	0	0	0	0	0	0	0
154	0	0	0	0	0	0	0	0	0	0
176	0	0	0	0	0	0	0	0	0	0
198	0	0	0	0	0	0	0	1	1	0
220	0	1	1	0	0	0	0	1	0	0

(c) 30 Minute Sample Logic Chart

Table A.4. Logic ON OFF Chart for Anealed Sphere Samples

Bibliography

1. O. James, “Electrical characterization of spherical copper oxide memristive array sensors,” Master’s thesis, Air Force Institute of Technology, 2014.
2. R. Anderson, *Security Engineering*, ch. 8, pp. 415–431. 2 ed., 2008.
3. O. if the Assistant Secretary of Defense for Nuclear Matters, *The Nuclear Matters Handbook*. 2011.
4. H. M. Jaeger, S. R. Nagel, and R. P. Behringer, “Behringer: Granular solids, liquids, and gases rev,” *Mod. Phys*, p. 187, 1996.
5. F. Sidoroff, B. Cambou, and A. Mahboubi, “Contact force distribution in granular media,” *Mechanics of Materials*, vol. 16, no. 1-2, pp. 83 – 89, 1993.
6. J. F. Peters, M. Muthuswamy, J. Wibowo, and A. Tordesillas, “Characterization of force chains in granular material,” *Phys. Rev. E*, vol. 72, p. 041307, Oct 2005.
7. S. Williams, “How We Found the Missing Memristor,” *IEEE Spectrum*, pp. 29–35, 2008.
8. W. Gary, “Memristive response of jammed granular copper array sensors to mechanical stress,” Master’s thesis, Air Force Institute of Technology, 2014.
9. L. Chua, “Memristor-the missing circuit element,” *Circuit Theory, IEEE Transactions on*, vol. 18, pp. 507–519, Sep 1971.
10. L. Chua and S. M. Kang, “Memristive devices and systems,” *Proceedings of the IEEE*, vol. 64, pp. 209–223, Feb 1976.

11. J. J. Yang, F. Miao, M. D. Pickett, D. A. A. Ohlberg, D. R. Stewart, C. N. Lau, and R. S. Williams, “The mechanism of electroforming of metal oxide memristive switches,” *Nanotechnology*, vol. 20, no. 21, p. 215201, 2009.
12. J. J. Yang, M. D. Pickett, X. Li, D. Ohlberg, D. R. Stewart, and S. R. Williams, “Memristive Switching Mechanism for Metal/Oxide/Metal nanodevices,” *Nature nanotechnology*, 2008.
13. D. B. Strukov, G. S. Snider, D. R. Stewart, and R. S. Williams, “The missing memristor found.,” *Nature*, 2008.
14. D. B. Strukov, J. L. Borghetti, and R. S. Williams, “Coupled ionic and electronic transport model of thin-film semiconductor memristive behavior,” *Small*, vol. 5, no. 9, pp. 1058–1063, 2009.
15. J. Livingston, *Electrical Properties of Engineering Materials*, ch. 1, pp. 3–17. 1999.
16. K. Fujiwara, T. Nemoto, M. J. Rozenberg, Y. Nakamura, and H. Takagi, “Resistance switching and formation of a conductive bridge in metal/binary oxide/metal structure for memory devices,” *Japanese Journal of Applied Physics*, vol. 47, no. 8R, p. 6266, 2008.
17. H.-S. Wong, H.-Y. Lee, S. Yu, Y.-S. Chen, Y. Wu, P.-S. Chen, B. Lee, F. Chen, and M.-J. Tsai, “Metal-oxide rram,” *Proceedings of the IEEE*, vol. 100, no. 6, pp. 1951–1970, 2012.
18. S. Zou, P. Xu, and M. Hamilton, “Resistive switching characteristics in printed cu/cuo/(ago)/ag memristors,” *Electronics Letters*, vol. 49, pp. 829–830, June 2013.

19. W. Smith, *Principles of Materials Science and Engineering*. McGraw-Hill series in materials science and engineering, McGraw-Hill, 1996.
20. A. S. Zoolfakar, R. A. Rani, A. J. Morfa, A. P. O'Mullane, and K. Kalantar-zadeh, "Nanostructured copper oxide semiconductors: a perspective on materials, synthesis methods and applications," *J. Mater. Chem. C*, vol. 2, pp. 5247–5270, 2014.
21. L. D. L. S. Valladares, D. H. Salinas, A. B. Dominguez, D. A. Najarro, S. Khondaker, T. Mitrelias, C. Barnes, J. A. Aguiar, and Y. Majima, "Crystallization and electrical resistivity of Cu_2O and CuO obtained by thermal oxidation of Cu thin films on SiO_2/Si substrates," *Thin Solid Films*, vol. 520, no. 20, pp. 6368 – 6374, 2012.
22. P. van der Heide, *X-Ray Photoelectron Spectroscopy: An Introduction to Principles and Practices*. Wiley, 2012.
23. M. C. Biesinger, L. W. Lau, A. R. Gerson, and R. S. Smart, "Resolving surface chemical states in {XPS} analysis of first row transition metals, oxides and hydroxides: Sc, Ti, V, Cu and Zn," *Applied Surface Science*, vol. 257, no. 3, pp. 887 – 898, 2010.
24. M. C. Biesinger, B. R. Hart, R. Polack, B. A. Kobe, and R. S. Smart, "Analysis of mineral surface chemistry in flotation separation using imaging {XPS}," *Minerals Engineering*, vol. 20, no. 2, pp. 152 – 162, 2007.
25. B. Castle, "Memristive properties of thin film cuprous oxide," Master's thesis, Air Force Institute of Technology.
26. "Industrial tectonics inc.," 2015.

27. R. Nisbett J.K. Budynas, *Shigleys Mechanical Engineering Design*. McGraw-Hill, 9 ed., 2011.
28. T. Driscoll, H. T. Kim, B. G. Chae, M. Di Ventra, and D. N. Basov, “Phase-transition driven memristive system,” *Applied Physics Letters*, vol. 95, no. 4, pp. 043503+, 2009.
29. K. M. Kim, D. S. Jeong, and C. S. Hwang, “Nanofilamentary resistive switching in binary oxide system; a review on the present status and outlook,” *Nanotechnology*, vol. 22, no. 25, p. 254002, 2011.
30. D. Feng and G. Jin, *Introduction to condensed matter physics*, vol. 1. World Scientific, 2005.
31. Y. Leng, *Materials Characterization: Introduction to Microscopic and Spectroscopic Methods*. Wiley, 2009.



REPORT DOCUMENTATION PAGE

*Form Approved
OMB No. 0704-0188*

The public reporting burden for this collection of information is estimated to average 1 hour per response, including the time for reviewing instructions, searching existing data sources, gathering and maintaining the data needed, and completing and reviewing the collection of information. Send comments regarding this burden estimate or any other aspect of this collection of information, including suggestions for reducing the burden, to Department of Defense, Washington Headquarters Services, Directorate for Information Operations and Reports (0704-0188), 1215 Jefferson Davis Highway, Suite 1204, Arlington, VA 22202-4302. Respondents should be aware that notwithstanding any other provision of law, no person shall be subject to any penalty for failing to comply with a collection of information if it does not display a currently valid OMB control number.

PLEASE DO NOT RETURN YOUR FORM TO THE ABOVE ADDRESS.

1. REPORT DATE (DD-MM-YYYY)	2. REPORT TYPE	3. DATES COVERED (From - To)
-----------------------------	----------------	------------------------------

4. TITLE AND SUBTITLE	5a. CONTRACT NUMBER
	5b. GRANT NUMBER
	5c. PROGRAM ELEMENT NUMBER

6. AUTHOR(S)	5d. PROJECT NUMBER
	5e. TASK NUMBER
	5f. WORK UNIT NUMBER

7. PERFORMING ORGANIZATION NAME(S) AND ADDRESS(ES)	8. PERFORMING ORGANIZATION REPORT NUMBER
--	--

9. SPONSORING/MONITORING AGENCY NAME(S) AND ADDRESS(ES)	10. SPONSOR/MONITOR'S ACRONYM(S)
	11. SPONSOR/MONITOR'S REPORT NUMBER(S)

12. DISTRIBUTION/AVAILABILITY STATEMENT

13. SUPPLEMENTARY NOTES

14. ABSTRACT

15. SUBJECT TERMS

16. SECURITY CLASSIFICATION OF:			17. LIMITATION OF ABSTRACT	18. NUMBER OF PAGES	19a. NAME OF RESPONSIBLE PERSON	
a. REPORT	b. ABSTRACT	c. THIS PAGE			19b. TELEPHONE NUMBER (Include area code)	